

---

# The Impact of Turbulence and Turbine Operating Condition on the Wakes of Tidal Turbines

Ebdon Tim <sup>1</sup>, Allmark Matthew J. <sup>1</sup>, O'doherty Daphne M. <sup>1</sup>, Mason-Jones Allan <sup>1</sup>, O'Doherty Tim <sup>1,\*</sup>, Germain Gregory <sup>2</sup>, Gaurier Benoit <sup>2</sup>

<sup>1</sup> Cardiff University, School of Engineering, The Parade, Cardiff, CF24 3AA, UK

<sup>2</sup> IFREMER, Marine and Structures Laboratory, Centre Manche Mer Du Nord, 150 Quai, Gambetta, 62200, Boulogne-sur-Mer, France

\* Corresponding author : Tim O'Doherty, email address : [odoherly@cardiff.ac.uk](mailto:odoherly@cardiff.ac.uk)

---

## Abstract :

Before initiating a study on the interaction of multiple wakes, it is imperative that turbine wake hydrodynamics are studied in isolation. In this paper CFD computer simulations of downstream turbine wakes have been run using a scale-resolving hybrid turbulence model known as a detached eddy simulation. To allow validation of the CFD simulations the computer models were supported by flume measurements with a lab scale tidal stream turbine run at three tip-speed ratios and three turbulence conditions, varying both turbulence intensity and length-scale.

From the study it was demonstrated that turbulence intensity has a significant impact on the wake development for both recovery and width. The turbulence length scales of between 0.25 and 1.0 rotor diameter did not have a significant impact on the wake.

The turbine operating condition also had an impact on the resulting wakes. In the near wake, centreline velocity recovery was found to increase with increasing turbine thrust due to flow being diverted towards the turbine nacelle. For a volumetric averaged wake, greater power extraction was found to cause the greatest near-wake deficit. Wake width was found to increase with increasing tip-speed ratio (and therefore turbine thrust).

## Highlights

► Wake widths and lengths for a tidal turbine using three different analysis metrics are presented. ► Three levels of turbulent conditions are presented using upstream grids. ► The impact of the turbine operating conditions, on the wake characteristics, are analysed. ► The impact of turbulence intensity and Integral length scales on the wake characteristics are analysed.

**Keywords :** Turbine Wake characteristics, Turbulence, Tip speed ratio, CFD modelling, Experimental analysis

## 29 1. INTRODUCTION

30 As with many industries reliant on the exploitation of fluid flows, the tidal stream turbine  
31 industry has used a combination of numerical modelling and scale testing in order to reduce  
32 the financial risks involved in installing full-scale turbines at tidal sites [1-5]. Much of the  
33 numerical modelling of tidal turbines has examined a diverse range of factors from blade  
34 design to flow-misalignment to ambient turbulence and their impacts on turbine performance  
35 [2, 3, 5]. Largely due to the computational costs associated with large, detailed models of  
36 turbines, the majority of this work has concentrated on the performance of individual,  
37 isolated turbines. In order to most effectively exploit the tidal stream resource, which is found  
38 in areas of limited geographical extent, tidal turbines are expected to be deployed in arrays,  
39 and the close proximity of turbines to one-another in these arrays has the potential to lead to  
40 interactions between them. In contrast to the wind, the tidal resource is highly predictable in  
41 both speed, direction and temporal variations [4]. Therefore, there is more potential for  
42 optimisation in the array layout of tidal stream turbines, by minimising detrimental  
43 interactions and maximising positive interactions between the turbines. In order to achieve  
44 this end, it is crucial to improve the current understanding of the physical processes occurring  
45 in the wake of tidal stream turbines by exploring what factors influence the size and shape of  
46 the wake, and what is the nature of the turbulent flow in the wake region. Knowledge of this  
47 will inform array layout, allowing the right compromises to be made in order to maximise

energy extraction whilst reducing turbine loading and capital costs, and minimising any potential impacts that turbine arrays might have on the wider environment. This can be achieved by building confidence in a numerical model of turbine wakes through validation against flume experiments and/or full-scale models and prototypes. These models can subsequently be used to explore a wider range of conditions experienced by the turbines to increase understanding of the interaction of wakes and turbines, leading to optimised array designs. To date, most modelling of tidal turbine wakes has been conducted using Reynolds-Averaged Navier-Stokes (RANS) turbulence models or vortex methods [1], however, these have been shown to overpredict the extent of the wake when compared to experimental measurements [6, 7], demonstrating the need for a different approach.

### 1.1 Wakes of isolated turbines

Early work on wake development was conducted by Lissamann [8] and Jensen [9]. Frandsen et al. [10] adapted the work of Jensen and applied it to arrays of offshore wind turbines. The ‘top-hat’ profile, which underestimates velocity deficit at the centre of the wake and overestimates it at the wake edges, was replaced by Bastankhah and Porté-Agel [11] with a Gaussian profile. Lam and Chen [12] combined axial momentum theory across an actuator disc with flume measurements from Maganga et al. [13] to develop analytical equations for the prediction of the axial velocity deficit and its lateral distribution downstream of a tidal turbine which were later adapted to include the effects of the turbine hub and predict the region of “double-dip” wake deficit seen in the near-wake region [14]. The improved equations showed good agreement with measurements made by Mycek et al. [15]. One of the earliest studies of the wake of a tidal turbine was conducted in a flume experiment by Maganga et al. [13]. They found that the turbulence intensity (TI) had a significant effect on the length of the wake.

Early numerical studies sought to reduce computational expense through the use of porous discs to simplify the geometry of a turbine, whilst still producing a wake. Models have been presented by Harrison et al. [16], Malki et al. [17] and Bai et al. [18], amongst others, which all combine an actuator disc approach with RANS-based CFD modelling for the flow field around and downstream of the disc. These steady-state models however fail to capture the transient effects in the near wake. Attempts to make the actuator disc model more closely match a physical turbine have been made by Nishino and Willden [19], to account for turbulence from the turbine blades, to more accurately reproduce the near wake mean flow.

Measurements have been made in the wakes of actuator discs [20] and in some cases behind individual turbines [13, 21, 22]. The work of Maganga et al. [13] showing that an increase in TI causes faster wake recovery, was confirmed by Mycek et al. [21], who concluded that, whilst an increase in ambient TI only had a limited effect on the mean power coefficient ( $C_p$ ) and thrust coefficient ( $C_T$ ), the wake was “deeply influenced” by the upstream turbulence, and that the “wake shape, length and strength largely depend on the upstream turbulence conditions”. Investigations into the turbulence produced in the near wake (between 1.5 and 7 diameters downstream of the rotor) were made by Tedds et al. [23] who noted that the rotation of the turbine blades induced significant anisotropy into the turbulence, and suggested that numerical models which rely on the assumption of isotropic turbulence may struggle to accurately reproduce the flow.

### 1.2 Interactions within small groups of turbines

As with studies on the wakes of single turbines, much of the initial research into blockage effects used actuator discs, either experimentally or using (Blade Element Momentum-CFD) BEM-CFD models [19, 24]. Turnock et al. [25] used a coupled BEM-CFD model to examine the effects of turbine separation both laterally and longitudinally. They found that a lateral spacing of 2 turbine diameters provided the highest power output from a row of turbine. This

97 has been supported by other studies using a BEM-CFD method [18, 26] and with full-rotor  
 98 RANS CFD [27]. These studies found that lateral spacing of  $2.5D$  [18] (where  $D$  represents  
 99 the diameter of a turbine) and  $2D$  [26, 27], gave the highest  $C_p$  for turbines in this row. It was  
 100 also found that a second row of turbines should be at least  $5D$  downstream of the first row  
 101 and staggered for the best overall performance [27].

102 The effects of lateral and longitudinal spacing on the wakes of tidal turbines has been  
 103 studied by Stallard et al. [28]. The study found that for lateral spacing  $\geq 3D$ , the wakes of the  
 104 individual turbines are unchanged from the case of an isolated turbine, but for spacing of  $\leq 2D$   
 105 the wakes from the individual turbine merge to form one single wake by  $4D$  downstream of  
 106 the rotors. Another study, this time using PIV measurement techniques, demonstrated the  
 107 complex nature of turbine interactions within an array [29]. This found that the lateral  
 108 spacing between turbines effected the array centreline wake recovery, potentially having a  
 109 detrimental impact on downstream turbines. Field tests of multiple turbines have also been  
 110 conducted to examine the interactions between turbines and the dependence on turbine  
 111 spacing by measuring the change in  $C_p$  due to the presence of a second turbine [30]. The  
 112 study examined both lateral and longitudinal spacing of two identical turbines, finding that  
 113 lateral a spacing of  $2D$  produced a performance increase of up to 6%. Due to the restrictions  
 114 on the towing rig used, a maximum longitudinal spacing of  $6D$  was measured, which revealed  
 115 a 59% reduction in performance, However, when the downstream turbine was offset by  $1.5D$   
 116 or  $3D$  from the centreline of the upstream turbine, no negative effects were observed, giving  
 117 an idea of the effective width of the wake.

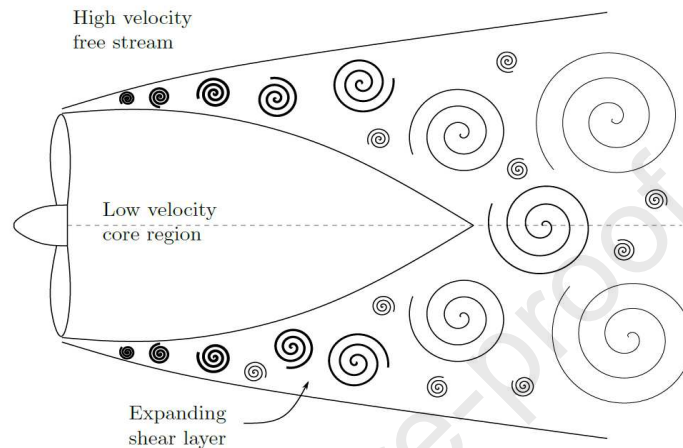
118 Other studies have examined the rate of wake recovery behind the turbine, both  
 119 numerically and experimentally [6, 13, 31, 32]. Examining the length of the wake's feeds into  
 120 considerations of longitudinal spacing of turbines within arrays. An increase in ambient  
 121 turbulence causes faster wake recovery [13, 20, 33-35]. Hence the position of a downstream  
 122 turbine will be dependent on the wake-length and width of an upstream turbine. However, the  
 123 characteristics of the turbulence is also important [13, 32]. As mentioned above, the  
 124 anisotropy in the wake induced by the turbine [7, 36, 37] has been investigated in the context  
 125 of arrays [27, 36] and found to have notable influence.

126

## 127 2 WAKE ANALYSIS METRICS

128 The length, width and characteristics of a wake are dependent on the shape of an object in  
 129 the flow [38], the nature of the flow and the fluid itself. The wake induced by the presence of  
 130 the object is a region of slower moving fluid with increased turbulence when compared to the  
 131 free-stream (Figure 1). Mixing takes place between the higher velocity free-stream and the  
 132 lower velocity wake, and the associated change in momentum causes the wake to gradually  
 133 return to the same velocity as the free-stream. This is known as wake recovery. Just behind  
 134 the object, the lower velocity wake and higher velocity free-stream regions are distinct from  
 135 one another, separated by a thin, highly sheared layer; flow recirculation is often observed in  
 136 this near wake region. As the fluid progresses downstream, momentum exchange takes place  
 137 across the shear layer, leading to wake recovery taking place from the outside towards the  
 138 centre. At the same time, the shear layer becomes thicker, extending outwards into the free-  
 139 stream and inwards towards the centre of the wake, whilst simultaneously decreasing in  
 140 strength. The overall area affected by the wake becomes wider, but the strength of the wake  
 141 itself (the velocity deficit) decreases. At some point downstream of the object, the shear layer  
 142 reaches the centreline of the wake. Beyond this point, the flow is still affected by the presence  
 143 of the object upstream, exhibiting increased turbulence and a remaining velocity deficit, but  
 144 the bounds of the wake become less defined. Eventually, very far downstream of the object,  
 145 viscous effects will damp down and dissipate any remaining turbulence and the wake will  
 146 continue to recover, until it is indistinguishable from the upstream flow.

147 This qualitative description of a wake will be recognised by flow physicists, but in order to  
 148 compare wakes, quantitative metrics must be developed. Clearly, an area of reduced flow  
 149 velocity and increased turbulence has the potential to impact downstream turbines through  
 150 reduced flow velocity and increased turbulence. Whilst the importance of being able to  
 151 quantify both the strength of the wake as well as the size of the region it affects is clear,  
 152 developing quantitative metrics by which to do this is more difficult. Developing quantitative  
 153 metrics is difficult because of the highly turbulent nature of the wake, meaning that the width  
 154 and length can fluctuate with time [39].



155

156 **Figure 1:** A schematic of the wake description. Flow direction is from left to right.

157

## 158 2.1 Wake length

159 In general, wake recovery occurs at a higher rate in the near wake, where the difference  
 160 between the velocities of the wake and the free-stream is greatest, and the exchange of  
 161 momentum is most effective. As the wake and free-stream become more similar to each  
 162 other, the effect of momentum mixing reduces, and the rate of recovery decreases and the  
 163 wake velocity approaches that of the free-stream in an asymptotic manner. For practical  
 164 measurements of wake length, it is necessary to take a velocity threshold where it can be said  
 165 that the wake has 'recovered'. The choice of this velocity threshold is essentially arbitrary,  
 166 but for the purposes of this work, a 90% wake recovery (10% deficit) is used. The paper will  
 167 use terms that are ubiquitous to the subject matter, but the authors will define some of the  
 168 terms next for clarity.

169

### 170 2.1.1 Centreline velocity recovery

171 The simplest, and most widely used, method of quantifying the length of the wake is by  
 172 analysing the recovery of the time-averaged axial velocity along the turbine centreline. This  
 173 has the advantage of being easily extracted from CFD modelling or measured experimentally.  
 174 However, it only provides information about the centreline axial velocity, and does not  
 175 contain any information about the distribution of velocity in the wake region - information of  
 176 critical importance to turbine and array developers. In addition to this, wake recovery occurs  
 177 from the outside towards the centreline, meaning that centreline measurements can  
 178 potentially under-estimate the level of wake recovery since the turbine blades are located  
 179 some radial distance from the centreline. Using this information alone could lead to a turbine  
 180 developer using an unnecessarily large downstream spacing for the layout of a turbine array,  
 181 reducing the amount of energy which can be extracted from a site of limited geographical  
 182 extent.

183

184

185 **2.1.2 Volumetric averaged velocity**

186 To account for the distribution of flow velocity behind the turbine, the volumetrically  
 187 averaged velocity has also been used. This is an area-weighted estimate of the time-averaged  
 188 axial velocity through the swept area of the turbine. This was recorded at regular intervals  
 189 downstream from the turbine and has been shown to give a better estimate of the energy  
 190 available to a downstream turbine [6]. This is trivial to extract from CFD data; the time-  
 191 averaged velocity is integrated over the swept area of the turbine at different downstream  
 192 stations. However, due to the time required to make measurements in a flume, these were  
 193 only taken on a horizontal plane. To obtain an estimate of the volumetric flow over the swept  
 194 area of the turbine, a shell (or disc) integration was performed on the measured velocity  
 195 profiles, following the procedure used by Mycek et al. [21]. The same procedure was also  
 196 carried out on the CFD data to provide comparative results.

197

198 **2.1.3 Wake width**

199 Initially, a turbine wake is approximately as wide at the turbine rotor itself. However, as  
 200 the wake develops downstream, mixing takes place between the high-velocity free-stream,  
 201 and the lower velocity wake region, causing a layer of sheared flow. Initially this shear is  
 202 high and the shear layer thin, but as the wake develops, the thickness of this shear layer  
 203 increases, and the velocity gradient (shear) decreases. This simultaneous change in both  
 204 thickness and strength of the shear layer makes a simple definition of a wake difficult. This  
 205 difficulty is only compounded by the fact that the turbine wake may meander in time [33, 35].  
 206 Therefore, three different methods have been proposed and used in the analysis of turbine  
 207 wakes in this paper:

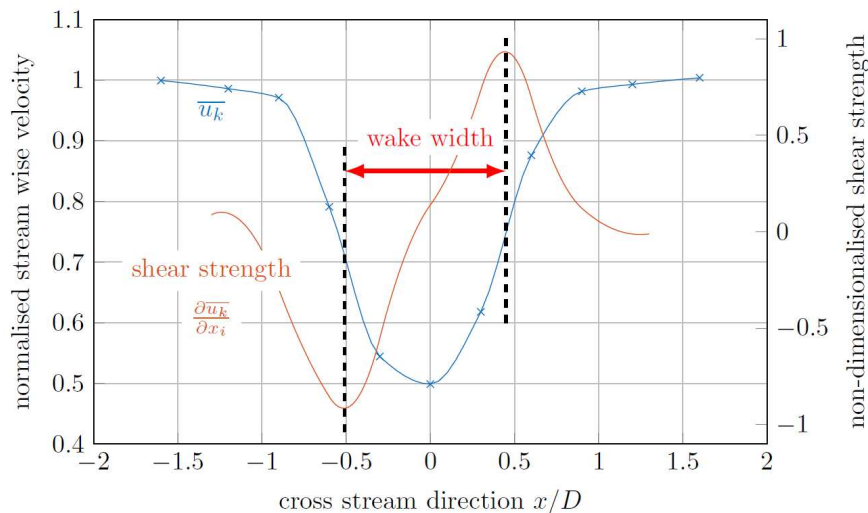
- 208 1) a width metric based on the point of maximum-shear,
- 209 2) a width metric based on a fixed velocity threshold, and
- 210 3) a width metric based on a full-width half minimum method.

211 All three methods have been designed to be implemented for measurements of time-averaged  
 212 axial velocity in a rake parallel to the plane of the turbine rotor.

213

214 **2.2 Wake width based on the point of maximum-shear**

215 In this case the position of the edges of the wake is defined by the point of maximum-shear  
 216 which is defined as the position with the greatest rate of change in the time-averaged axial  
 217 velocity in the cross-stream direction. As shown in Figure 2, the wake width is then the  
 218 distance between the points at which this shear is a maximum.

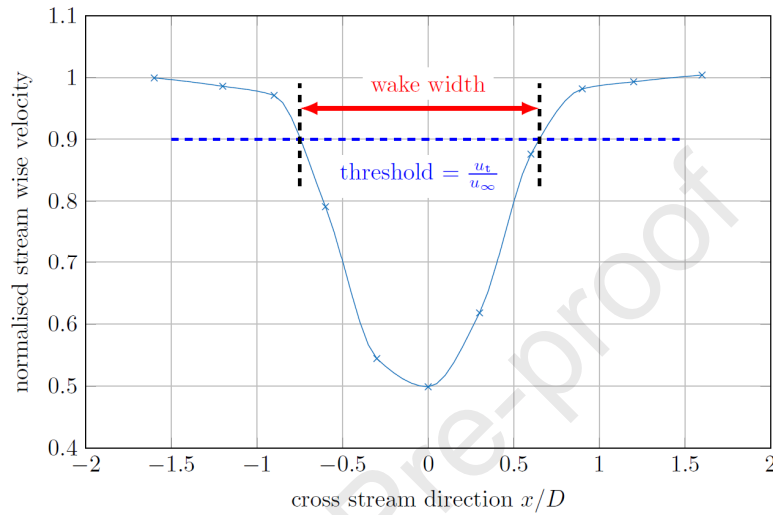


219

220

**Figure 2:** Wake width: the maximum-shear method.**2.3 Wake width based on a fixed velocity threshold**

222 For array designers, a more useful definition of wake width may be the width of the region  
 223 with a velocity deficit above a certain threshold, i.e. 90% wake as stated earlier (Figure 3). As  
 224 the wake recovers from the outside inwards due to the mixing of momentum from the free-  
 225 stream, it is expected that the wake width will decrease as it develops downstream of the  
 226 turbine. Once all of the wake has recovered to more than 90%, the wake width will become  
 227 zero [40].

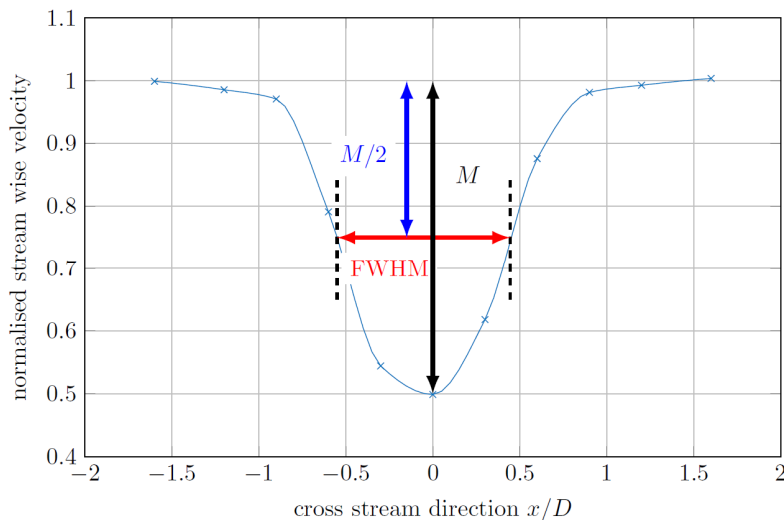


228

229

**Figure 3:** Wake width: the fixed velocity threshold method.**2.4 Wake width based on the full-width half-minimum of the velocity deficit**

231 A third approach, which recognises that the width of the region affected by the wake  
 232 increases even as the velocity deficit decreases, is taken by a width measurement metric  
 233 based on the idea of a full-width half-minimum (Figure 4). The full-width half-maximum is a  
 234 concept often used in statistics and signal processing to analyse the width of a peak. This  
 235 method is also a velocity threshold, but the threshold at a particular downstream position is  
 236 chosen as half of the maximum velocity deficit at that downstream position in the wake,  
 237 rather than being a fixed proportion of the free-stream velocity. Once half of the maximum  
 238 velocity deficit has been calculated, the width is calculated as the cross stream extent of the  
 239 wake which has a velocity deficit equal to this value.



240

241 **Figure 4:** Wake width: Full-Width Half-Minimum (FWHM) method.

### 242 **3 TURBINE AND EXPERIMENTAL SETUP**

243 The turbine used for this work was a 0.5 m diameter three-bladed, horizontal axis design,  
 244 with blades based on a Wortmann FX 63-137 section. The blades have a twist of  $30^\circ$  from  
 245 root to tip and were attached to a 100 mm diameter hub via root stubs and grub screws. The  
 246 details of the rotor geometry and outputs has been reported in detail elsewhere [6, 37, 41-44].  
 247 The turbine nacelle was 763 mm long and a maximum diameter of 160 mm. The turbine hub  
 248 is directly connected to a Bosch Rexroth type MST130E-0035 synchronous torque motor  
 249 which is housed within the nacelle along with a slip ring, and associated electronics for  
 250 control and instrumentation. Electric power and sensor cables are routed out of the  
 251 downstream face of the nacelle. The motor torque was measured via the electrical current  
 252 required to either drive or brake the turbine. For all the experiments detailed in this paper, the  
 253 constant rotational velocity mode was used, replicating the constant rotational velocity used  
 254 in the CFD study. The turbine assembly is suspended under water by means of a 71 mm  
 255 diameter stanchion.

#### 256 **3.1 Sensors, data recording and instrumentation**

257 The turbine was designed for physical testing to measure loads on, and power output of a  
 258 turbine, with a specific focus on condition monitoring [44] but has also been used for work  
 259 investigating the impact of misalignment [45], and surface waves. Data acquisition (as well  
 260 as turbine control) was carried out using a National Instruments PXIe-8135 embedded  
 261 controller and PC. A sample rate of 200Hz was used, which allowed 41s of data to be  
 262 sampled. This gives a sample rate identical to that from the CFD simulations, with data being  
 263 sampled over a similar amount of time to the 50s simulated numerically.

#### 264 **3.2 Uncertainty analysis**

265 Uncertainty analysis was conducted for the turbine performance characteristics of  $C_p$ ,  $C_T$   
 266 and  $C_\theta$ . Detailed uncertainty analysis used in the commissioning of the turbine are provided  
 267 by Allmark [44]. When collecting the data for the power curves presented in this paper, the  
 268 upstream velocity was not simultaneously measured, but characterised before the tests.  
 269 Subsequently the flume pump set-point used in the wake measurements was used. Hence, the  
 270 reference velocity used for the calculation of  $C_p$ ,  $C_T$  and  $C_\theta$  was based on a mean velocity.

#### 271 **3.3 Flume description**

272 Testing was carried out in the flume facility of the Institut Francais de Recherche pour  
 273 l'Exploitation de la Mer (IFREMER) in Boulogne-sur-Mer. A description of the flume can be  
 274 found in [21]. This recirculating flume has a working section 4m wide, 2m deep and with a  
 275 useable length of approximately 18m. It is capable of flow speeds of  $0.1\text{-}2.2\text{ms}^{-1}$ , but for  
 276 turbine testing was only used to a maximum of  $1.5\text{ms}^{-1}$ .

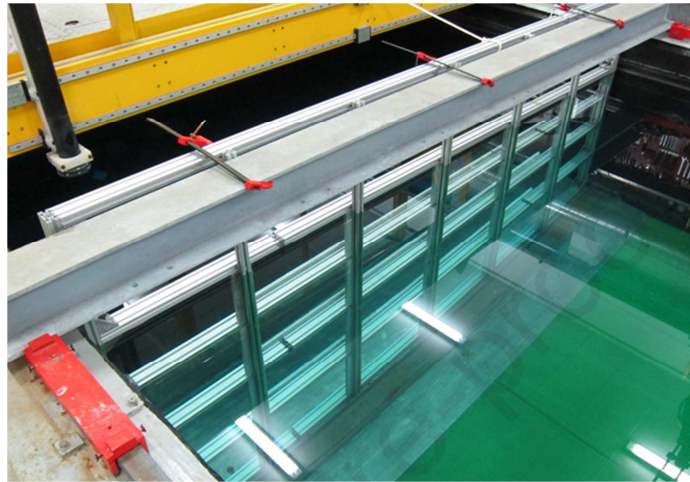
#### 277 **3.4 Flow measurement techniques**

278 Flow measurement was made using a 2D DANTEC FiberFLOW two-axis Laser Doppler  
 279 Velocimeter (LDV) system and calibrated  $\pm 0.001\text{ ms}^{-1}$ . The LDV system was attached to a  
 280 2D traverse and allowed the measurement procedure to be automated in the cross stream and  
 281 vertical directions. The measurement positions and times were pre-programmed, allowing  
 282 measurements to be made for one downstream station (in a plane perpendicular to the turbine  
 283 axis), before being moved to the next downstream position with errors of the order of  $\pm 5\text{ mm}$ .  
 284 Relative position errors in the cross-stream direction were of the order of  $\pm 1\text{ mm}$ .

#### 285 **3.5 Flow conditions**

286 Flume testing was conducted in three stages. Each stage sought to examine the wake under  
 287 three different types of flow condition; a low turbulence condition (1.75%), obtained using all

288 available flow-smoothing at the tank, and two test sets which used grids constructed of  
 289 aluminium frames and marine plywood and placed upstream of the turbine to induce  
 290 turbulence (Figure 5). The dimensions of the grids followed those used by Blackmore et al.  
 291 [46]. In their study length scales of between 0.18 - 0.82 m were achieved, approximately  
 292 0.35-1.5 times the diameter of the turbine rotor studied in this paper. Using grids about which  
 293 data had already been published allowed an estimation of the TI and length scales to be  
 294 expected before going to the flume. The grids were installed by fastening it to the base of the  
 295 flume and an I-beam above the surface of the water.  
 296



297  
 298  
 299 **Figure 5:** The fine grid installed in the IFREMER flume, viewed from downstream  
 300

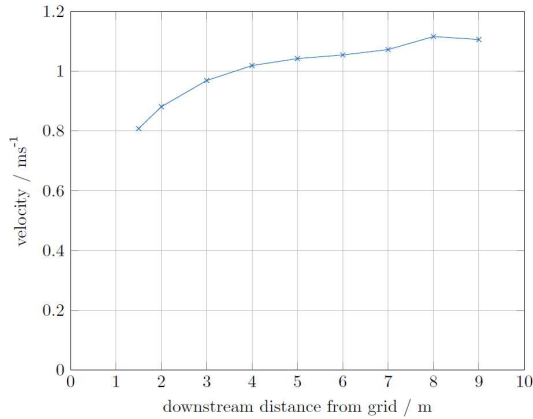
301 Before installing the turbine in the flume, the flow downstream of the grid was  
 302 characterised. This was done via a sequence of LDV measurements in the centre of the cross  
 303 sectional area of the flume. These were carried out for 1000s each, in order to obtain high  
 304 confidence in the higher-order statistics. Plots showing velocity, TI and integral length scale  
 305 ( $L_T$ ) with distance downstream of the grid are shown in Figures 6a-c respectively for the fine  
 306 grid, and 6d-f for the coarse grid. Error bars have been omitted from these figures for clarity,  
 307 as in all cases 95% confidence intervals were less than 0.5% of the values shown. The figures  
 308 for the fine grid show that the velocity behind the grid increases with downstream distance  
 309 (most likely due to the near-grid velocity being affected by the position of individual bars,  
 310 with this effect becoming less influential as downstream distance increases), TI decreases  
 311 with downstream distance, showing the dissipation of turbulence, and integral length scale  
 312 tends to increase, indicating the dissipation of the shorter length scales with time. Based on  
 313 the analysis of flow development behind the grid, as well as consideration of the space  
 314 required to carry out wake measurements, the turbine rotor was placed at 4m downstream of  
 315 the fine grid.

316 The figures for the coarse grid show similar trends to that of the fine grid, albeit as  
 317 anticipated with a higher TI and greater turbulence length scale. No measurements were made  
 318 closer than 5m from the grid, as the TI was measured to be over 30% at this point. The  
 319 turbine was placed 9m downstream of the coarse grid, as this was the greatest distance that it  
 320 could be placed from the grid, whilst still leaving enough space downstream of the turbine for  
 321 wake measurements.

322 Once the centreline measurements had been made and the turbine position chosen, flow  
 323 uniformity across the swept area of the turbine was assessed by re-measuring at the chosen  
 324 position on the flume centreline, as well as  $\pm 0.25\text{m}$  in both the horizontal and vertical  
 325 directions, at the limits of the turbine swept area. Each of these measurements was made for

326 500s and show the flow to be reasonably uniform across the turbine swept area, with the  
 327 integral length scale being approximately that of the turbine rotor radius behind the fine grid  
 328 and that of the turbine rotor diameter behind the coarse grid. Turbulence generated from these  
 329 grids can be expected to be largely isotropic (in the vertical and transverse directions). It is  
 330 worth noting that turbulence at potential tidal sites is unlikely to be isotropic [47 - 50],  
 331 however, the specific turbulence characteristics will be specific to individual sites and would  
 332 need to be investigated in detail.

333

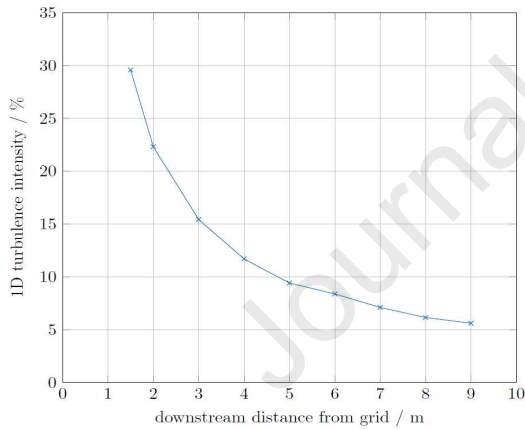


334

a: Velocity behind the fine grid

335

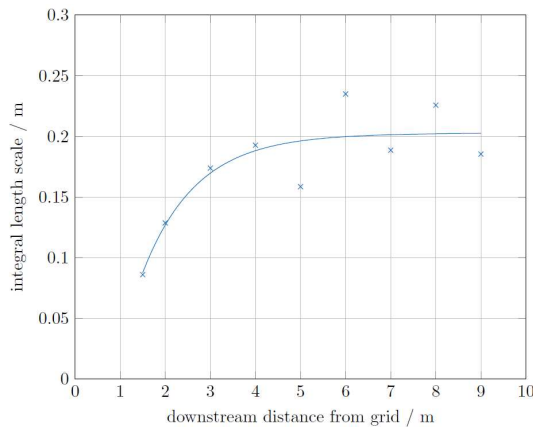
336



337

338 b: 1D turbulence intensity behind the fine  
 339 grid

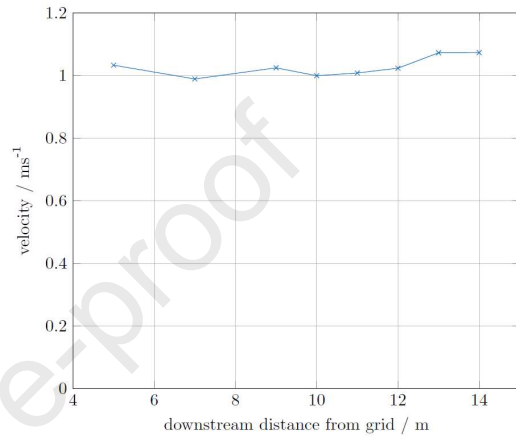
340



341

342 c: Integral length scale behind the fine grid

343

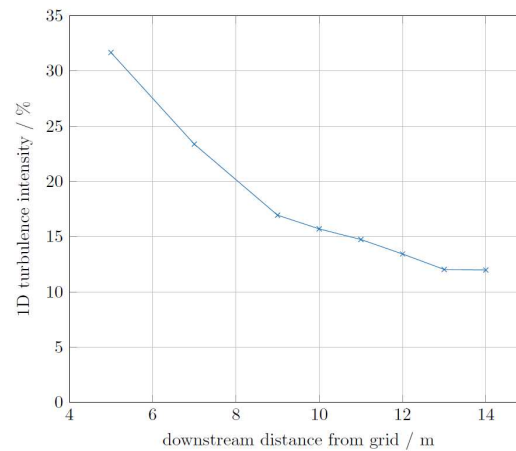


344

d Velocity behind the coarse grid

345

346



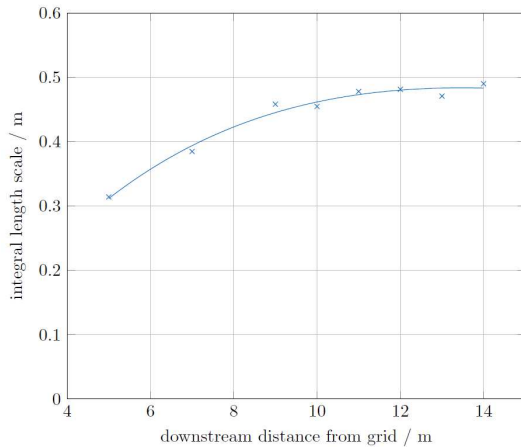
347

348

349

350

e: 1D turbulence intensity behind the  
 coarse grid



352 f: Integral length scale behind the coarse  
 353 grid  
 354

351

355 Figure 6: Flow characteristics downstream of the fine and coarse grids, measured at the centre  
 356 of the cross-sectional area of the flume.

357 For the test conducted in the low turbulence conditions without any grid, vertical profiles of  
 358 axial velocity and TI were made across the region where the turbine was present. This showed  
 359 the velocity to vary by  $\pm 1.5\%$  and the TI by  $\leq 2\%$  across the diameter of the turbine, indicating  
 360 a low turbulence, highly uniform flow. A summary of the flow conditions and tip-speed ratios  
 361 for which wake measurements were made can be seen in Table 1.

362

Table 1 Test flow conditions at the turbine rotor position.

Grid		None	Fine	Coarse
Distance from grid / m		n/a	4.0	9.0
Velocity / $\text{ms}^{-1}$		1.5	1.02	1.03
1D Turbulence intensity / %		1.75	11.7	17.5
Integral length scale / m		0.5	0.19	0.43
Tip-speed ratios tested	2.5		X	X
	3.65	X	X	X
	4.5		X	X

363

## 364 4. CFD METHODOLOGY

### 365 4.1 CFD setup, geometry and boundary conditions

366 The work contained within this thesis was conducted using the commercial CFD code  
 367 Ansys Fluent. Fluent uses a finite volume method for solving the continuity and momentum  
 368 equations for fluid flow. Flume-scale simulations were carried out using Fluent 18.0 on HPC  
 369 facilities at Cardiff University.

370 Simulation of the rotating turbine was achieved via a sliding mesh scheme as used by  
 371 Morris [37]. This involves the creation of two separate domains, with two independent  
 372 meshes. For the turbine, a cylindrical domain is created within the main domain,  
 373 encompassing the rotating parts of the turbine. This cylinder is then physically rotated with  
 374 each timestep, in accordance with the pre-determined rotational velocity. The mesh of the  
 375 rotating domain and the main domain are not necessarily conformal, and the two meshes slide  
 376 past each other at the mesh boundaries. This scheme allows for flow interactions between the  
 377 turbine blades and stanchion and allows these cyclic interactions and the resultant wake to be  
 378 evaluated.

379 The turbine was suspended in the centre of the cross-sectional area of a flume, with a width  
 380 of 4 m and depth of 2 m, giving a blockage ratio by turbine swept area of approximately

381 2.5%. The CFD domain extended 1.5 m upstream of the rotor, and 7.5 m downstream,  
 382 representing a modelled domain of from  $z/D = -3$  to  $z/D = 15$ . The upstream domain boundary  
 383 was set as a constant velocity inlet with specified turbulent conditions, including the addition  
 384 of synthetic turbulent perturbations. Inlet turbulence was specified via turbulence intensity  
 385 and a length scale, described by Ansys as representing the length scale of the turbulence  
 386 features containing the most energy; similar to the definition of the integral length scale [46].  
 387 Production of turbulence perturbations using this method is based on a Biot-Savart rule, and  
 388 1000 seed vortices were chosen, in keeping with the Ansys recommendation that the number  
 389 of seed vortices should be approximately  $\frac{1}{4}$  the number of cell faces at the inlet.

390 The downstream domain boundary was a constant pressure boundary with a gauge pressure  
 391 of 0 Pa. A zero-shear condition was applied to the upper domain boundary rather than  
 392 representing a free surface, in common with other low-blockage numerical simulations. All  
 393 other boundaries (both flume walls and turbine) were treated as stationary no-slip walls, using  
 394 the default roughness coefficient of 0.5.

395 A comprehensive mesh independence study was carried out by varying the mesh densities  
 396 in the area immediately around the turbine rotor, the nacelle region, the wake region, and the  
 397 surrounding volume of fluid. The resulting mesh contained a total of  $11.38 \times 10^6$  cells and is  
 398 detailed in [51].

## 399 4.2 Turbulence model

400 To date, the majority of numerical research on tidal turbines and their wakes has been  
 401 conducted using RANS turbulence models. These models recognise that, for most engineering  
 402 flows, users are more interested in the time-averaged values of flow variables such as  
 403 velocity, than the instantaneous values. RANS models are based on the idea that the  
 404 instantaneous value of a flow variable, e.g. velocity, can be represented by its mean and a  
 405 fluctuating component. This process is known as Reynolds decomposition, and is represented  
 406 mathematically in equation 1, where  $U$  is the time-averaged flow velocity, and  $u'(t)$  represents  
 407 the fluctuating component of velocity.

$$408 \quad u(t) = U + u'(t) \quad (1)$$

409 The Reynolds-decomposed variables are then substituted into the incompressible 3-  
 410 dimensional Navier-Stokes equations. This yields the time-averaged Navier-Stokes equations  
 411 for  $U$ , which are formally identical to the Navier-Stokes equations for instantaneous flow  
 412 variables, with an additional term, shown in equation 2, and known as the Reynolds stresses.  
 413 Here  $u'_i$  and  $u'_j$  represent instantaneous velocity components in the  $i$  and  $j$  directions  
 414 respectively,  $\rho$  represents density, and  $\tau_{ij}$  represents the tensor stress component in the  $ij$   
 415 direction.

$$416 \quad \tau_{ij} = -\rho \overline{u'_i u'_j} \quad (2)$$

417  
 418  
 419 The Reynolds stresses represent the exchange of momentum between the mean and the  
 420 fluctuating flow components, and must be modelled in order to close the Navier-Stokes  
 421 equations and obtain a solution for  $U$ . Various schemes have been developed for the  
 422 modelling of the Reynolds stresses, each with differing levels of complexity, from the mixing  
 423 length model, through two-equation models such as the  $k-\varepsilon$  and  $k-\omega$  through to the Reynolds  
 424 Stress Model, which requires seven equations to be solved for closure to be achieved [52].

425 The advantage of RANS equations is that they provide a good compromise between  
 426 computational cost and accuracy. They are well characterised, and it is known which ones

427 perform best for different types of flow. Variations such as the  $k-\omega$  SST model exist, which  
428 attempt to combine the best characteristics of the  $k-\varepsilon$  and  $k-\omega$  models. However, these models  
429 struggle with flows which demonstrate a large turbulence length scale or a high degree of  
430 turbulence anisotropy like that shown to be present in the wake of a tidal turbine [23]. This is  
431 thought to be due to the reliance of two-equation RANS models on the Boussinesq  
432 approximation, which assumes isotropy of turbulence. This assumption is usually valid for  
433 small-scale turbulence, but it becomes less appropriate for larger turbulent length scales [48],  
434 such as those found at potential tidal energy sites [53]. In addition to this, the focus on time  
435 averaged values means that some data regarding fluctuating quantities is unavailable.

436 A different approach to accounting for turbulent fluctuations is provided by Large Eddy  
437 Simulation (LES). This approach applies a spatial filter to the Navier-Stokes equations, with  
438 fluctuations larger than the filter width (typically the local cell size) being resolved, and  
439 fluctuations smaller than the filter width being treated with a sub-grid scale model, in a way  
440 analogous to a RANS model. LES allows for much more information to be gathered about  
441 fluctuating quantities than RANS models. This is because the fluctuations themselves (or at  
442 least, the large ones) are directly resolved, allowing the user to carry out their own statistical  
443 analysis on them, in a way similar to how measurements in a flume would be analysed. In  
444 addition to this, treating large and small eddies differently means that LES can accurately  
445 model flows with large turbulence anisotropy and length scales. However, LES is  
446 significantly more computationally expensive than two-equation RANS models for two main  
447 reasons; firstly, LES has higher mesh requirements in boundary regions, and secondly, in  
448 order for converged statistical values of fluctuating quantities to be obtained, the model must  
449 be run for significantly more time steps.

450 The DDES (Delayed Detached Eddy Simulation) method used in this work is a hybrid  
451 turbulence model which endeavours to combine the advantages of LES in the wake region  
452 with RANS in near-wall areas in order to more accurately model the wake, whilst reducing  
453 computational expense to less than would be required for a pure LES model. This is achieved  
454 by recognising that, once averaging has been carried out (time averaging in the case of RANS,  
455 or spatial averaging for LES), information about the averaging method is lost, and both RANS  
456 and LES models become turbulence viscosity models. The DDES model compares the local  
457 turbulence length scale to the local cell size and uses this to decide to what extent the  
458 turbulence viscosity of the model should be modified from that obtained from a  $k-\omega$  SST  
459 model (if at all). This results in a RANS model being applied in near wall areas, and LES-like  
460 behaviour being recovered in the wake region. Due to space requirements, the mathematics of  
461 the model will not be described in detail here, as the necessary information has been  
462 previously detailed in [47] and [54].

## 463 **5 TURBINE PERFORMANCE, EXPERIMENTAL**

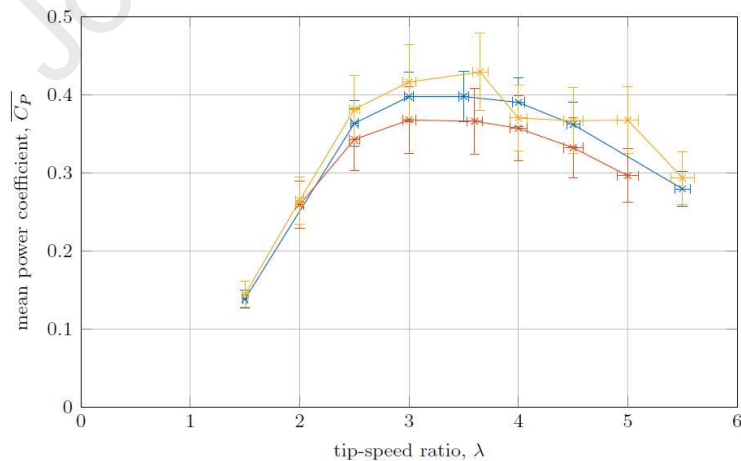
464 Uncertainties were calculated using standard procedures[55, 56] and applying central limit  
465 theorem to quantities which have been obtained by averaging multiple samples of a  
466 population. These have been applied to measurements of flow velocity, turbulence intensity  
467 and turbine performance. Where error bars are displayed on charts, they represent confidence  
468 intervals of 95%. Where error bars are not displayed, they have either not been calculated (in  
469 the case of numerically integrated quantities such as  $L_t$  which would require very advanced  
470 methods to calculate and are beyond the scope of this work) or the calculated bounds of the  
471 95% confidence intervals were within 1% of the reported value. In these cases, they have been  
472 omitted for clarity. Both CFD and experimental data are presented as curves, with crosses

473 marking the positions where an experimental measurement was taken. If error bars are  
 474 present, then the crosses may have been omitted, for clarity.

### 475 5.1 Flume results, lab scale turbine

476 Plots of  $C_P$ ,  $C_T$  and thrust coefficient ( $C_\theta$ ) for the low turbulence, medium turbulence and  
 477 high turbulence cases are shown in Figures 7a, b, c. Information regarding  $C_T$  was only  
 478 available from the low-turbulence tests. The thrust data was determined via strain gauges on  
 479 the stanchion at a clamping point above the waterline, so producing a bending moment from  
 480 the force acting on the turbine and stanchion. It has therefore been included for indicative  
 481 purposes but does not provide data for direct comparison with the CFD results, as these record  
 482 the force on the turbine blades and hub only. Error bars on  $C_P$  and  $C_\theta$  have been calculated  
 483 using the procedure outlined in [45], with an assumed uncertainty in the mean velocity of  
 484  $\pm 0.02 \text{ ms}^{-1}$ , due to the use of the flume set-point rather than making simultaneous  
 485 measurements of the flume velocity.

486 The curves of  $C_P$  and  $C_\theta$  from the flume experiments show agreement, within the  
 487 experimental uncertainties, between all three turbulence cases, demonstrating the same trends  
 488 and similar magnitudes for all cases. As found in previous experimental work with this  
 489 turbine, the position of maximum  $C_P$  was found to occur at  $\lambda = 3.65$ , with maximum torque  
 490 occurring at  $\lambda = 2.5$ . Nonetheless, it appears that the medium-turbulence case has, in general,  
 491 the lowest  $C_P$ , the high-turbulence case the highest  $C_P$ , and the low-turbulence case between  
 492 the two. This could be an indication of transition effects in the boundary layer of the turbine  
 493 blades. As the  $Re$  at which the blade is operating is around the point of transition from  
 494 laminar to turbulent flow. In general, it might be expected that an increase in turbulence,  
 495 which will disrupt the flow over the turbine blade, will lead to a decrease in turbine  
 496 performance, explaining the drop in performance from the low-turbulence case to the  
 497 medium-turbulence case. However, due to the transitional nature of the boundary layer, it is  
 498 possible that a separation bubble is being formed in these cases. With the large amount of  
 499 turbulence in the high-turbulence case, it is unlikely that any separation bubble will survive  
 500 due to the increase of energy in the boundary layer. If separation does not take place, then it is  
 501 possible that, the turbine performance will actually increase in the high-turbulence case,  
 502 reflecting the behaviour seen in Figure 7a.



503  
 504

a

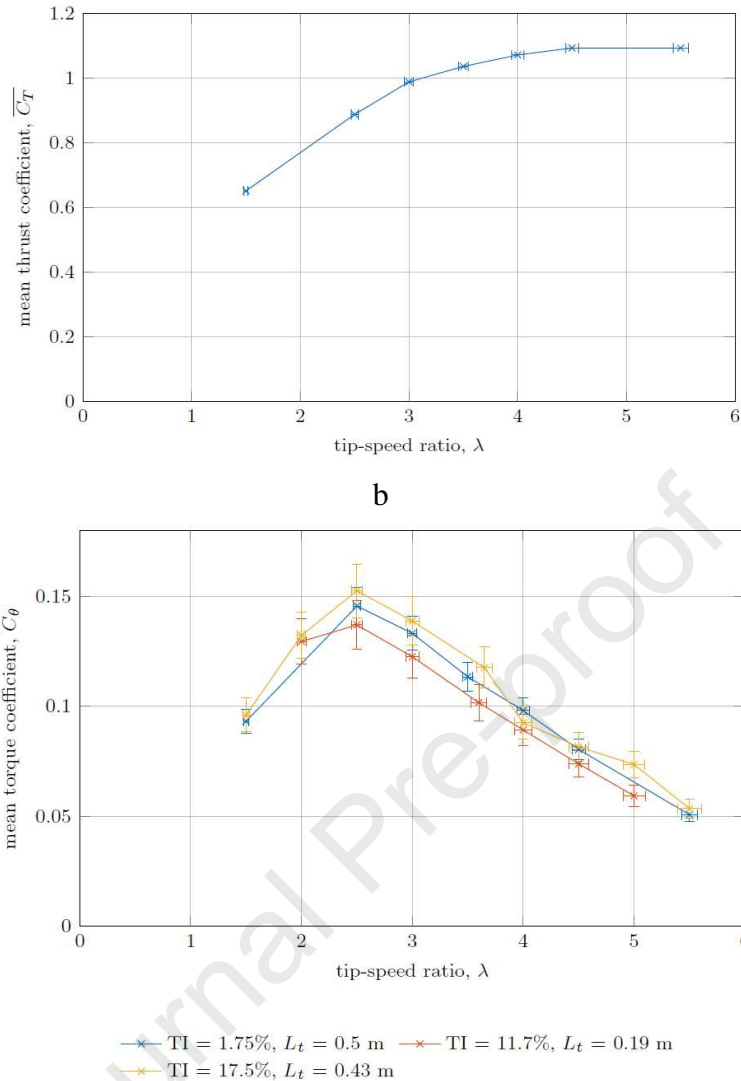


Figure 7 Flume results for a)  $C_P$  vs.  $\lambda$ . b)  $C_T$  vs.  $\lambda$ . c)  $C_\theta$  vs.  $\lambda$

## 5.2 Wake recovery

### 5.2.1 CFD results

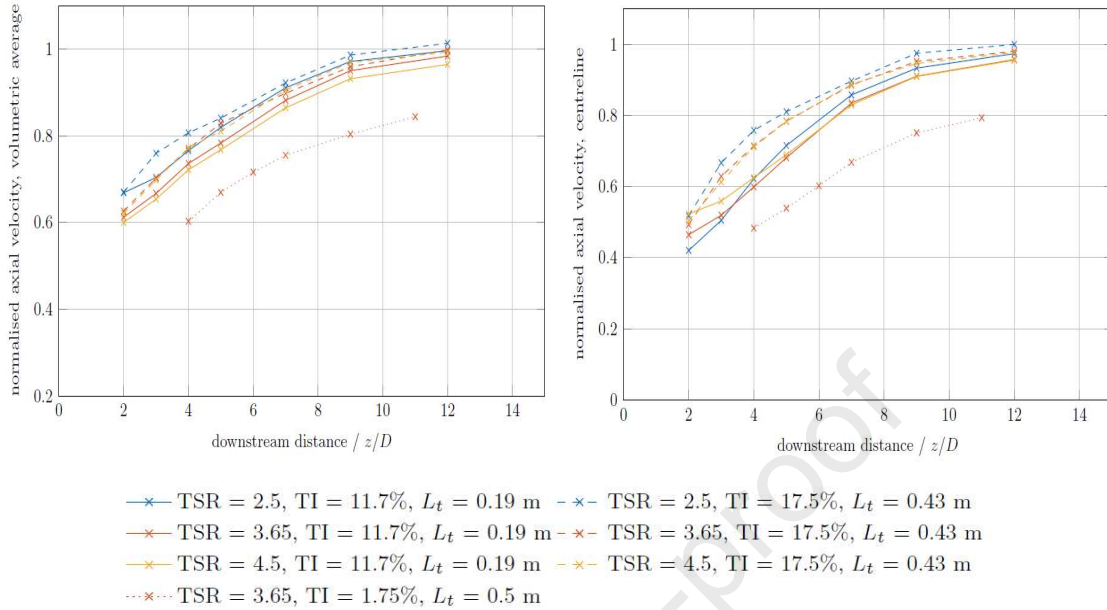
Wake recovery will be primarily examined using centreline and volumetric averaged wake recovery curves, Figure 8. However, in order to fully understand some of the effects and impacts (particularly the impact of  $\lambda$  on the wake width), it is useful to present wake profiles for a typical case. Figures 9 present wake profiles for the low-turbulence CFD conditions. These profiles show that the shape of the wake is dependent on  $\lambda$ ; with low  $\lambda$ , low-thrust cases leading to v-shaped wake profiles, and high  $\lambda$ , high-thrust cases leading to wake profiles which approximate a top-hat shape, the highest thrust cases leading to profiles with three minima.

### 5.2.2 Flume results

Results for the low TI, fine grid and coarse grid tests were analysed, with the centreline (Figure 8a), and volumetric averaged velocity recovery (Figure 8b).

Both of these figures show a clear trend - that higher TI is associated with faster wake recovery. This is expected, and follows trends found in previous experimental studies [13, 21]. Further to this, for the tests using grid-generated turbulence, the three  $\lambda$  values were used, and a trend is also apparent in all cases;  $\lambda = 2.5$  shows the fastest overall recovery, with  $\lambda =$

527 3.65 and  $\lambda = 4.5$  showing similar rates of wake recovery. This would appear to then show a  
 528 similar trend to that shown by the  $C_T$  curve (Figure 7b) with a larger difference between the  
 529 thrust at  $\lambda = 2.5$  and  $\lambda = 3.65$ , than between the  $\lambda = 3.65$  and  $\lambda = 4.5$  cases.



530

531

532

a) Centreline wake recovery.

b) Volumetric averaged wake recovery

533

534

**Figure 8:** Wake recovery for flume measurements at all measured tip-speed ratios and turbulence intensities.

535

536

537

538

539

540

541

542

543

544

545

546

547

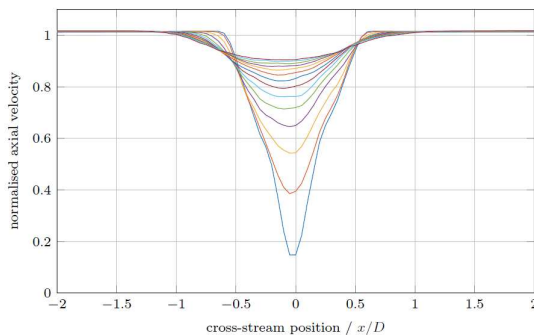
548

549

550

551

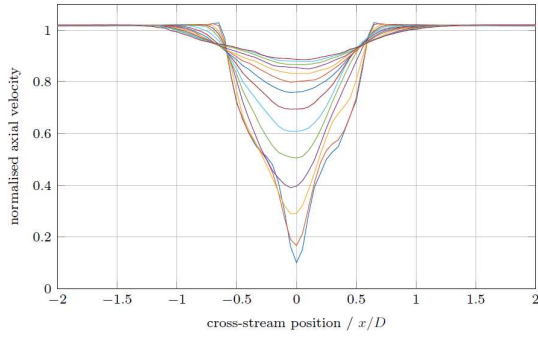
As expected for a wake recovering due to mixing with the free-stream, the centreline velocity (Figure 8a) is consistently lower than the volumetric average velocity (Figure 8b) until approximately  $z/D=9$  downstream of the turbine, where the normalised velocities becomes similar, regardless of which metric is used. This suggests that by this point the wake region has become homogeneous, and that the mixing layer has reached the centreline. One area of interest is the near wake ( $z/D \leq 4$ ) centreline recovery for the turbine downstream of the fine grid. In this region, the  $\lambda = 2.5$  case is less recovered than the  $\lambda = 3.65$  or  $4.5$  cases, in contrast to the overall trend for the rest of the wake. This suggests that the  $\lambda = 2.5$  wake is demonstrating a large amount of inhomogeneity in this near wake region. This could be due to the fact that the blades in the  $\lambda = 2.5$  case are producing less thrust, and therefore the influence of the nacelle is greater, leading to a lower velocity core when compared to the rest of the wake region. In addition to this, the  $\lambda = 2.5$  case has the greatest rotational motion in the wake, which could be hindering wake mixing in this near-wake region. This trend is not apparent in the highest TI case, but this could be due to the greater level of turbulence leading to more mixing, making this effect less apparent. This is supported by CFD results presented in section 6.3.



53

a:  $\lambda = 1.5$ .

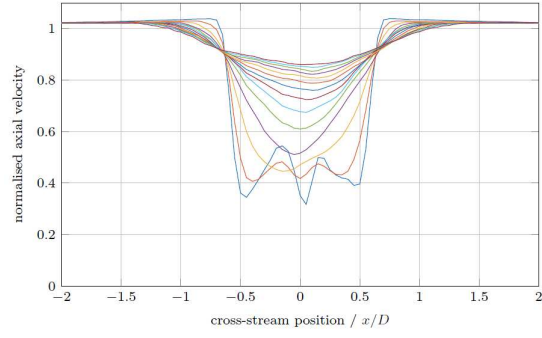
552



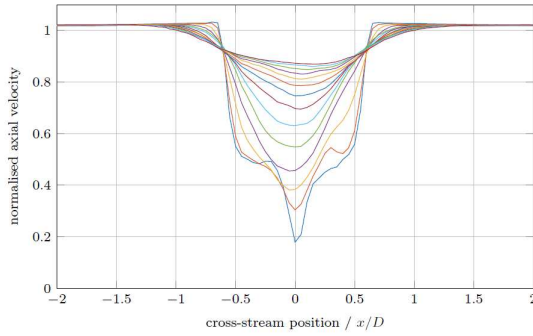
554  
555

**b:**  $\lambda = 2.5$ .

50  
561



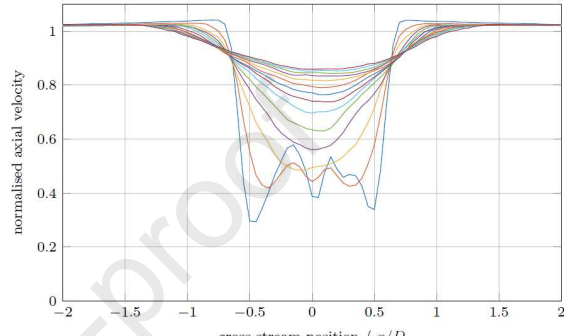
**e:**  $\lambda = 4.0$ .



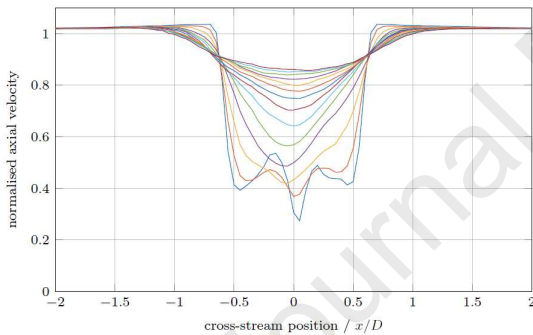
556  
557

**c:** for  $\lambda = 3.0$ .

562  
563



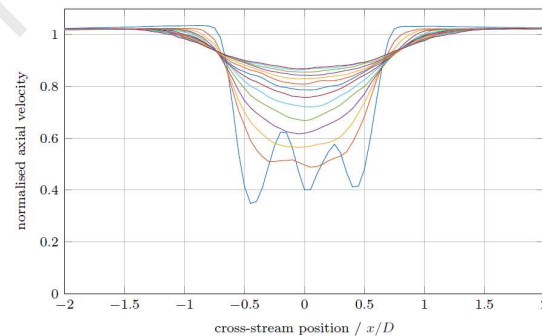
**f:** for  $\lambda = 4.5$ .



558  
559

**d:**  $\lambda = 3.65$ .

564  
565



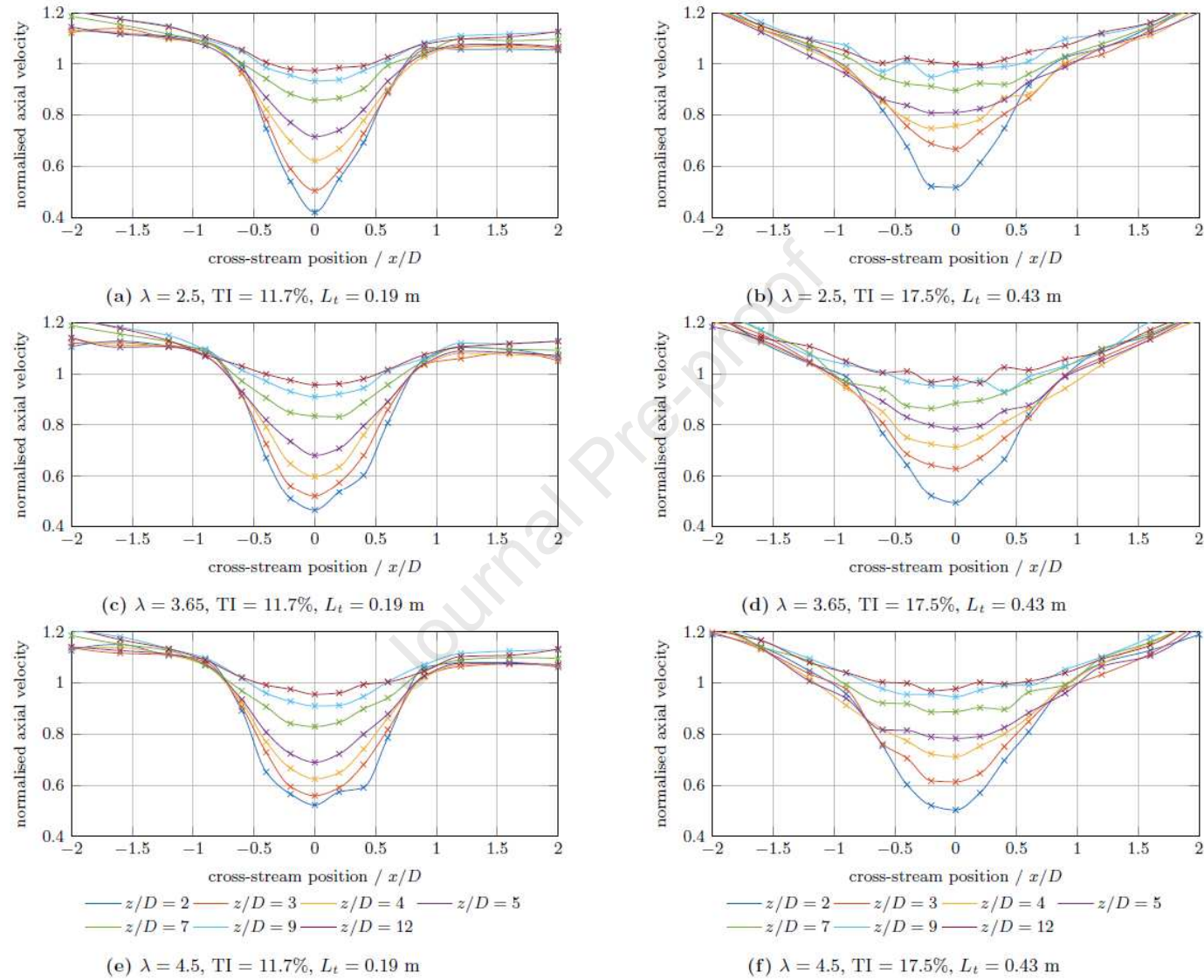
**g:**  $\lambda = 5.5$ .

—  $z/D = 2$  —  $z/D = 3$  —  $z/D = 4$  —  $z/D = 5$  —  $z/D = 6$   
 —  $z/D = 7$  —  $z/D = 8$  —  $z/D = 9$  —  $z/D = 10$  —  $z/D = 11$   
 —  $z/D = 12$  —  $z/D = 13$  —  $z/D = 14$  —  $z/D = 15$

566  
567

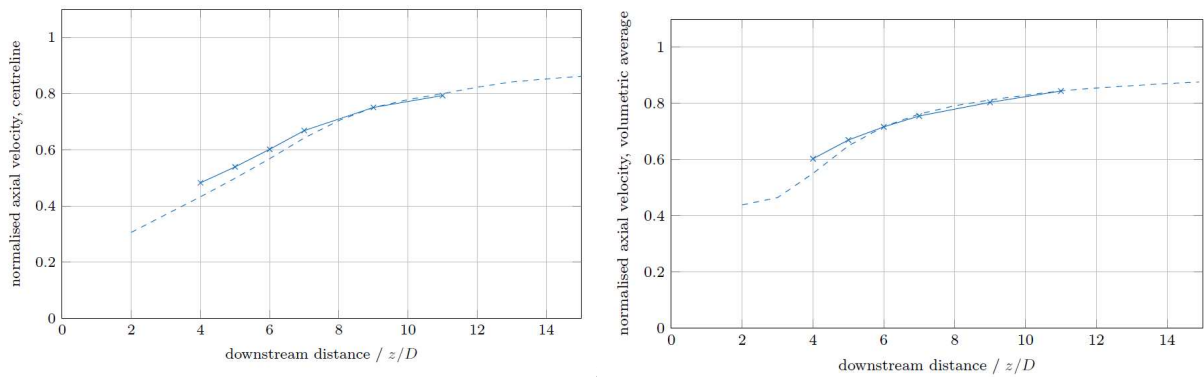
568 **Figure 9:** CFD wake profiles for the low-  
569 turbulence intensity

570

571  
572

**Figure 10:** Wake profiles for the fine- (subfigures a, c, e) and coarse-grid (subfigures b, d, f) flume cases.

573



574

575

**a: centreline wake recovery.**

577

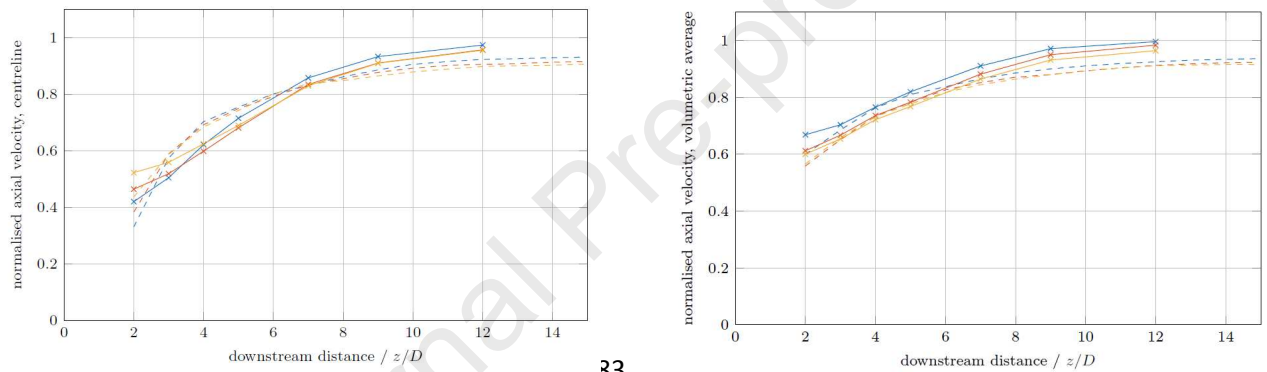
**b: volumetric wake recovery.**

—×— TSR = 3.65, TI = 1.75%,  $L_t = 0.5$  m, flume  
 - - - TSR = 3.65, TI = 0.96%,  $L_t = 0.8$  m, CFD

578

579

Figure 11: Validation of low turbulence CFD



580

581

582

**a: centreline.**

583

584

**b: Volumetrically averaged**

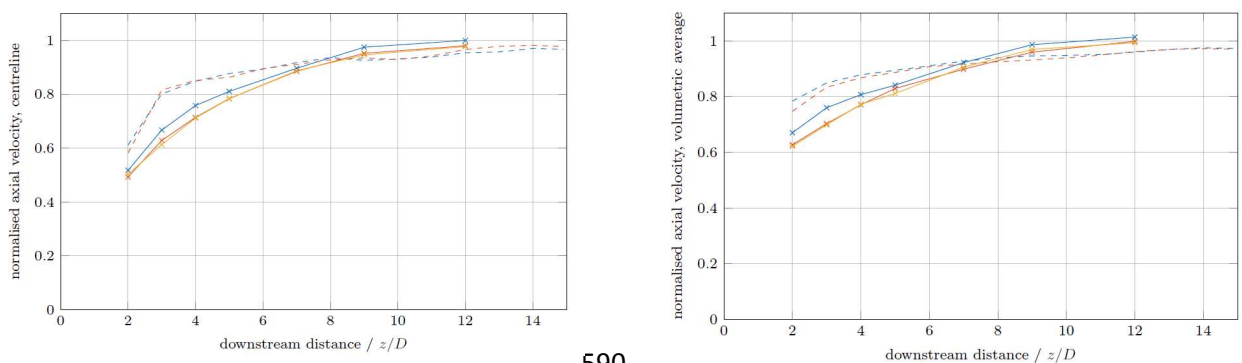
585

—×— TSR = 2.5, TI = 11.7%,  $L_t = 0.19$  m, flume    - - - TSR = 2.5, TI = 11.4%,  $L_t = 0.19$  m, CFD  
 - - × - - TSR = 3.65, TI = 11.7%,  $L_t = 0.19$  m, flume    - - - TSR = 3.65, TI = 12.4%,  $L_t = 0.20$  m, CFD  
 - - \* - - TSR = 4.5, TI = 11.7%,  $L_t = 0.19$  m, flume    - - - TSR = 4.5, TI = 12.4%,  $L_t = 0.20$  m, CFD

586

587

Figure 12: Wake recovery validation using flume results with the fine grid



588

589

**a: centreline**

590

591

**b: volumetric averaged.**

—×— TSR = 2.5, TI = 17.5%,  $L_t = 0.43$  m, flume    - - - TSR = 2.5, TI = 16.6%,  $L_t = 0.41$  m, CFD  
 - - × - - TSR = 3.65, TI = 17.5%,  $L_t = 0.43$  m, flume    - - - TSR = 3.65, TI = 14.6%,  $L_t = 0.41$  m, CFD  
 - - \* - - TSR = 4.5, TI = 17.5%,  $L_t = 0.43$  m, flume

592

593

Figure 13: Wake recovery validation using flume results with the coarse grid.

## 5.2.2 Validation of CFD

Validation of the CFD for prediction of wake recovery is made for the low turbulence case by comparison of flume results to CFD along the centreline (Figure 11a) and for volumetric averaged wake recovery (Figure 11b). These both show good agreement in the region for which both CFD and flume data are available, with excellent agreement from  $z/D = 8$  for the centreline recovery, and from  $z/D = 6$  for the volumetric averaged recovery. It can be expected that the volumetric-averaged method will provide slightly better matching, as the combination of area-averaging as well as time-averaging makes this metric less sensitive to slight changes in the velocity distribution within the wake. The small discrepancies between flume and CFD results in the near-wake region can be explained by the fact that the flow field in this region is likely to be more complex and thus more difficult to accurately reproduce in a simulation. Mixing and recovery in the far wake is likely to be dominated by the outer shear layer of the wake, and therefore less dependent on the mesh directly around the turbine nacelle. This suggests that the DDES model has the ability to provide accurate predictions of the recovery of a turbine wake from at least the mid-wake region, in low-ambient turbulence conditions.

The validation plots for wake recovery for the tests behind the fine grid are presented in Figure 12a for the centreline wake, and Figure 12b for the volumetric averaged wake. As with the low TI case, agreement is better in the volumetric averaged wake, again probably due to the combination of both time and area-averaging. Agreement is generally good, although deteriorates beyond approximately  $z/D = 7$ , where the CFD under predicts the recovery by approximately 8%. The difference in recovery rates for the different  $\lambda$  values is well reproduced; in the volumetric-averaged recovery  $\lambda = 2.5$  recovers faster than the other two cases, which show similar rates of recovery, with a tendency for the  $\lambda = 3.65$  case to recover slightly faster than the  $\lambda = 4.5$  case. Along the centreline, this trend of  $\lambda$  values showing faster recovery is reversed in the near wake region, but this is reflected in both the CFD and the flume results. At a downstream distance of  $3 \leq z/D \leq 5$ , the trend in wake recovery with  $\lambda$  reverts to that seen in the volumetric averaged wakes. Whilst the agreement between CFD and flume results behind the fine grid may not be quite as close as in the low-turbulence case, this is to be expected as it is unlikely that the CFD domain inlet will exactly reproduce the precise turbulence characteristics of the flume.

The validation plots for wake recovery for the testing campaign behind the coarse grid are presented in Figure 13a for the centreline wake, and Figure 13b for the volumetric averaged wake. Agreement in the mid- and far-wake is good, with a tendency for the CFD to slightly under-predict the recovery in the far wake, albeit only by around 5%. The CFD also tends to overpredict the recovery at distances of  $z/D \leq 6$ . As with the two previous flow conditions, the near-wake may be better reproduced with a finer mesh in the near-turbine region, but the discrepancies could also be explained by the high level of turbulence, and the CFD not exactly reproducing the turbulence characteristics of the grid-generated turbulence.

## 6 IMPACT OF TURBULENCE ON WAKE RECOVERY

### 6.1 Turbulence intensity

The impact of ambient TI on wake recovery is examined using the results in Figures 8 for flume centreline and volumetric averaged velocities. In addition, four selected CFD cases were compared which have similar turbulence conditions to each other except in respect of TI. The flume results with higher TI exhibiting more rapid wake recovery for both centreline and volumetric averaged results (Figures 8). For the volumetric averaged wake recovery curves, the wakes produced behind the fine grid and those behind the coarse grid still show only a slight difference, suggesting that there may be an upper limit beyond which an increase in TI has little further effect on wake recovery.

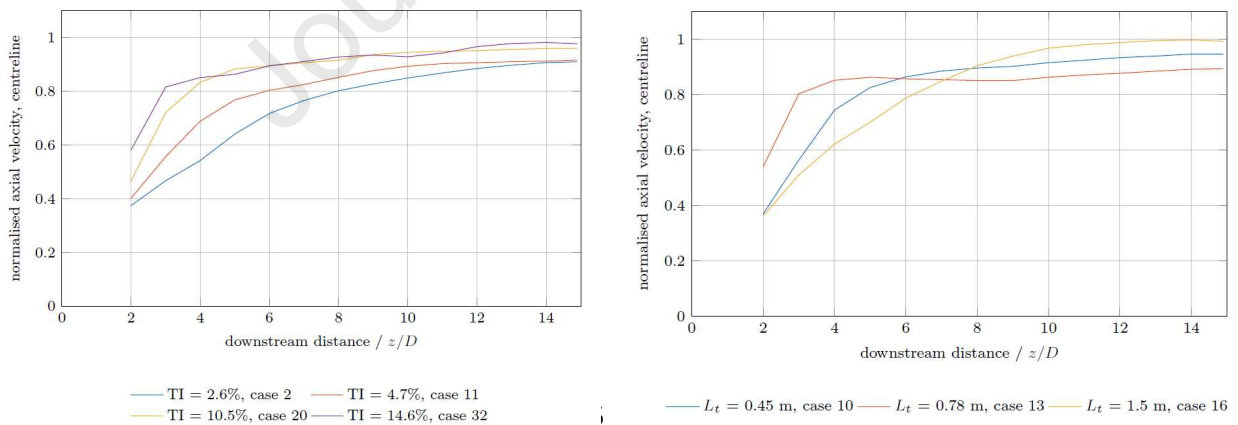
644 The CFD results are in general agreement with the flume results, with the figures for  
 645 centreline and volumetric averaged wake showing very similar behaviour (Figures 11 - 13).  
 646 Here it can also be seen that a higher TI promotes faster wake recovery, with the two cases of  
 647 greatest TI showing similar results from the mid-wake onwards. These results follow trends  
 648 seen in previous experimental work [13, 21], with the consensus being that higher ambient  
 649 turbulence promotes mixing and transfer of momentum across the wake shear layer,  
 650 increasing the velocity of the wake region, and promoting wake recovery.

## 651 6.2 Turbulence length scale

652 The impact of turbulence length scale on wake recovery was explored using three selected  
 653 CFD runs. The results are presented in Figures 14 for the centreline and volumetric averaged  
 654 wake recovery, respectively. In both cases the medium  $L_t$  case (0.78 m) initially shows a fast  
 655 recovery to approximately 90% of the free-stream velocity, after which very little further  
 656 recovery takes place. From  $z/D = 8$  the case with the largest  $L_t$  (1.5 m) shows the greatest  
 657 recovery. The cases with the smaller  $L_t$  sizes (0.45 and 0.78 m), showing a reduced rate of  
 658 recovery. This suggests that  $L_t$  may have an impact in the far wake as the case presented with  
 659 the largest  $L_t$  also has the lowest TI, which would tend to reverse the order seen in the far  
 660 wake.

661 In the near- to mid-wake ( $z/D < 7$ ), the shortest  $L_t$  has a faster centreline recovery than the  
 662 largest  $L_t$ , however, this trend is reversed for the volumetric averaged recovery. This could  
 663 indicate that the short length scales increase mixing within the wake region (and therefore  
 664 promote centreline wake recovery) in the near wake, with the larger length scales dominating  
 665 the mixing between the wake and the free-stream, which ends up dominating overall wake  
 666 recovery. The effect of momentum transfer across the outer shear-layer of the wake will first  
 667 be apparent in the volumetric-averaged recovery, with this trend reaching the centreline later.  
 668 This could indicate that larger length scales lead to slower initial, but faster overall wake  
 669 recovery. Nonetheless, the behaviour is complex and is difficult to completely isolate the  
 670 effects of  $L_t$  and TI. In addition, this study only compares three different length scales,  
 671 making non-linear effects difficult to identify.

672



673

674

a: ambient turbulence intensity

676

b: ambient turbulence length scale

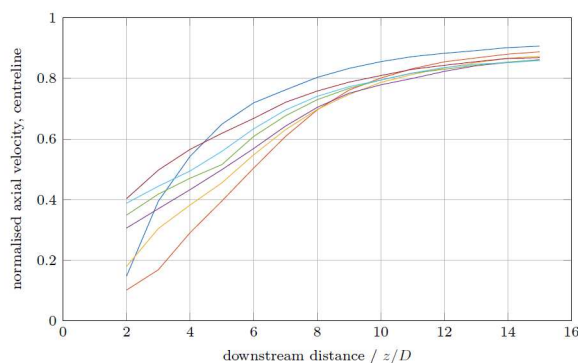
677 **Figure 14:** Impact of a) ambient turbulence intensity and b) length scale on centreline wake  
 678 recovery, CFD cases.

## 679 6.3 Impact of tip-speed ratio on wake recovery

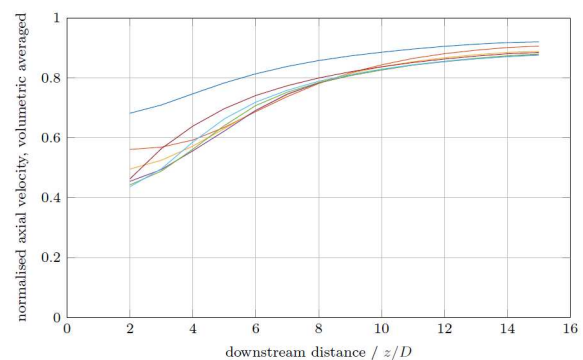
680 The impact of turbine operating condition on wake recovery can be examined using Figures  
 681 15 which examines the impact on the volumetric averaged wake recovery. The example  
 682 shown is from CFD in the low-turbulence case at  $\lambda = 3.65$  (Appendix: Table A.1, runs 34 -

683 40). Comparison of the two metrics allows assertions to be made about the homogeneity of  
 684 the velocity distribution in the wake region. If the trends are similar, this suggests a more  
 685 homogeneous wake, where they are not, which indicates that the velocity has a strong  
 686 dependence on radial position.

687 The centreline velocity recovery shows a clear trend with tip-speed ratio. The higher the  
 688 tip-speed ratio, the greater the initial wake recovery. Nonetheless, beyond approximately  $z/D$   
 689  $= 10$ , the tip-speed ratio seems to have little impact on the centreline wake recovery. This  
 690 appears to follow the trend of the thrust curve of the turbine, with higher thrust cases showing  
 691 a higher centreline recovery. This might appear counter intuitive, as a turbine with higher  
 692 thrust will be presenting more resistance to the flow, causing flow to divert around the rotor  
 693 swept area. However, most of the thrust is produced by the outer portion of the blades,  
 694 causing flow to be diverted not only outside and around the swept area, but also inwards  
 695 towards the blade roots and nacelle. This increases the velocity towards the centreline,  
 696 encouraging centreline wake recovery. This effect can be seen by comparing Figures 9a-g,  
 697 showing the wake velocity profiles for tip-speed ratios of  $1.5 \leq \lambda \leq 5.5$ , at downstream  
 698 positions from  $2 \leq z/D \leq 15$ . Low-thrust, low tip-speed ratios have profiles which are v-  
 699 shaped, but as the tip-speed ratio and thrust increases, the shapes of the wake profiles become  
 700 more like an inverted top-hat, with the highest-thrust cases exhibiting 3-dips in the nearest  
 701 profiles. The peaks between these dips indicate flow being diverted inwards, towards the  
 702 turbine nacelle, leading to the wake recovery curves seen in Figures 15. This trend in the  
 703 shapes of wake profiles with tip-speed ratio agrees with the wake profiles measured in the  
 704 flume, presented in Figure 10. The triple-dip profile at  $z/D = 2$  is not seen in these profiles  
 705 from the flume; however, given the much higher levels of turbulence and increased recovery  
 706 it is to be expected that this level of detail in the profiles may not be seen. Indeed, the change  
 707 in profile shape becomes less clear between the fine grid (Figures 10a, 10c and 10e) and  
 708 coarse grid case (Figures 10b, 10d and 10f). An exception to the overall trend is the  $\lambda = 1.5$   
 709 case. In the very near wake, this curve appears to approximately fit the trend for tip-speed  
 710 ratio, but thereafter recovers at a much greater rate than any of the other curves, such that, by  
 711  $z/D = 5$ , it has shown the most recovery - a trend which continues further downstream. Frost  
 712 provided detailed characteristics of the turbine and showed that at a tip-speed ratio of  $\lambda = 1.5$   
 713 the turbine is operating in the stall-region [45]. A stalled blade can be expected to produce  
 714 increased turbulence in the near-wake region than an un-stalled blade (due to flow separation  
 715 over the blades themselves), contributing to more mixing in this region, whilst at the same  
 716 time producing less thrust. Given this, it might be expected that the influence of the turbine  
 717 nacelle might be greater in the very near wake for the  $\lambda = 1.5$  case than for other tip-speed  
 718 ratios, but that the effect of increased blade turbulence causes rapid mixing and consequently  
 719 rapid wake recovery.



721 **a: centreline**



723 **b: volumetric averaged.**

— TSR = 1.5 — TSR = 2.5 — TSR = 3.0 — TSR = 3.65  
 — TSR = 4.0 — TSR = 4.5 — TSR = 5.5

724

725

**Figure 15:** Impact of TSR on wake recovery for low ambient turbulence condition.

726

727

728

729

730

731

The volumetric-averaged wake recovery curves presented in Figure 15b show a slightly different trend, whereby the  $\lambda$  values with the highest  $C_P$  tend to show the largest deficit in the near wake. This makes sense as the high  $C_P$  cases will extract more energy from the flow, by means of reducing flow velocity. Nonetheless, this effect is only apparent in the near-wake; beyond  $z/D \sim 4$ , all cases except for  $\lambda = 1.5$  and  $\lambda = 5.5$  are virtually indistinguishable from each other, with the  $\lambda = 5.5$  case merging at  $\sim z/D = 8$ .

732

733

734

735

736

737

738

As with the centreline wake recovery, the  $\lambda = 1.5$  case appears to be an outlier, showing greater wake recovery than any other case. This case has the lowest power and thrust coefficients of all of the cases in the figure, meaning that the turbine neither extracts much energy from the flow, nor provides great resistance to it. This leads to flow passing through the turbine swept area without being slowed down, and hence the wake is well recovered. A comparison of Figures 15 shows that the  $\lambda = 1.5$  case is highly inhomogeneous in the near wake, with a low velocity centreline surrounded by an otherwise well recovered wake.

739

740

741

742

743

744

For array designers, the most important conclusion to be drawn from Figure 15b is that (with the exception of the stalled case of  $\lambda = 1.5$ ) beyond  $z/D = 8$ , tip-speed ratio has little impact on the volumetric-averaged wake recovery. This means that even in the case where a turbine uses an over-speed regime to maintain rated power, there will be no impact on the longitudinal spacing (assuming the turbines are separated by at least 8D).

745

## 7 WAKE WIDTH

746

### 7.1 Flume results

747

748

749

750

751

Flume results for the wake width using the fixed-threshold, full-width half-minimum and maximum-shear methods are shown in Figures 16. Examining Figure 16a for the fixed-threshold method, it can be seen that, for all cases, the wake at  $z/D = 2$  is between 1-1.5D in width, with the width decreasing as the wake develops. This is to be expected as the fixed-threshold wake method is intrinsically linked to the wake recovery.

752

753

754

755

756

757

758

759

760

761

762

763

764

765

766

767

768

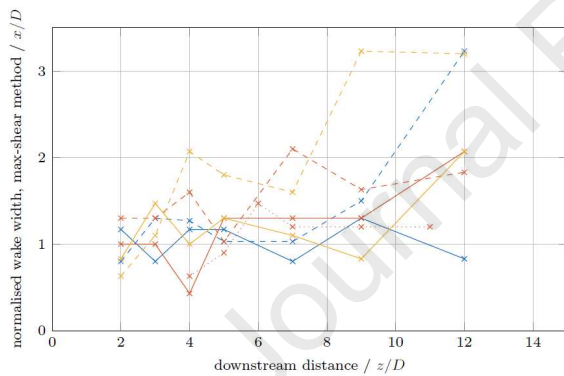
769

770

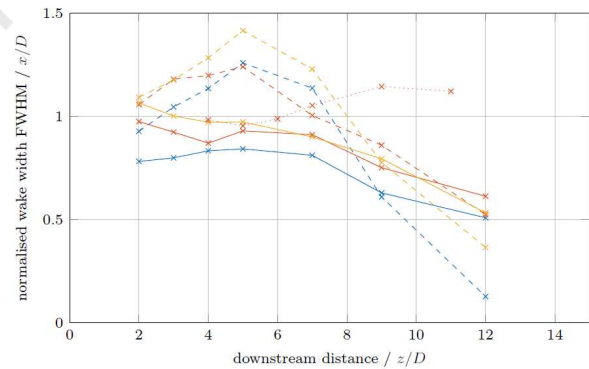
Recalling that the fixed-threshold method measures the width of the wake region which is less than 90% recovered, it is clear that, as the wake recovers, the region which is less than 90% recovered will tend to decrease. Assuming that recovery is symmetrical about the centreline, when the centreline velocity recovery reaches 90% of the free-stream, the wake width using this metric will become zero. This connection between wake recovery and fixed-threshold wake width explains the differences between the low-turbulence case ( $TI = 1.75\%$ ) and the cases behind the coarse and fine grids. The centreline wake recovery (Figure 8a) shows that both grid-generated turbulence cases demonstrate 90% wake recovery in the region  $7 \leq z/D \leq 9$ , whereas the low-turbulence case has only achieved approximately 80% recovery by  $z/D = 11$  downstream, where the measurements ended. This lack of mixing and recovery in the low-turbulence case explains why the wake persists for longer, leading to a wake that retains its width for longer (Figures 16a 16b). It appears that a higher ambient TI leads to a slightly greater wake width in the near wake region, but the coarse and fine grid cases ( $TI = 11.7\%$  and  $17.5\%$  respectively) show little difference from one another beyond  $z/D = 6$ . In addition to this, for the cases of grid-generated turbulence, there appears to be a dependence of wake width on tip-speed ratio, with greater  $\lambda$  leading to slightly wider wakes throughout their entire length. This is thought to be due to increased thrust on the turbines at the higher  $\lambda$  causing more flow to divert sideways and around the turbine, increasing the wake width.

771 A greater thrust on the turbine will tend to divert the oncoming flow outside and around the  
 772 turbine swept area, causing a wider wake. The wake width results following the full-width  
 773 half-minimum method for all flume cases are presented in Figure 16b. The shapes of the  
 774 curves are slightly different to those seen in Figure 16a as the two metrics are affected in  
 775 different ways by the shapes of the velocity profiles, however, the major trends from the  
 776 fixed-threshold method are also apparent in the full-width half-minimum method. The same  
 777 dependence of wake width on tip-speed ratio is apparent, with higher tip-speed ratios (and  
 778 therefore higher thrust) leading to wider wakes. In addition to this, as before, the width of the  
 779 wake in the low-turbulence case seems to persist for much further downstream than in the  
 780 higher-turbulence cases. It is thought that this is due to less mixing being present, allowing  
 781 the wake to maintain its shape further downstream. Again, as in the fixed-threshold case, the  
 782 wake width in the high-turbulence case is initially highest of all, perhaps due to increased  
 783 mixing broadening the shear layer between the wake and the free-stream. As the wake  
 784 develops downstream, the high-turbulence case seems to narrow at a faster rate than the other  
 785 cases, possibly due to increased mixing.

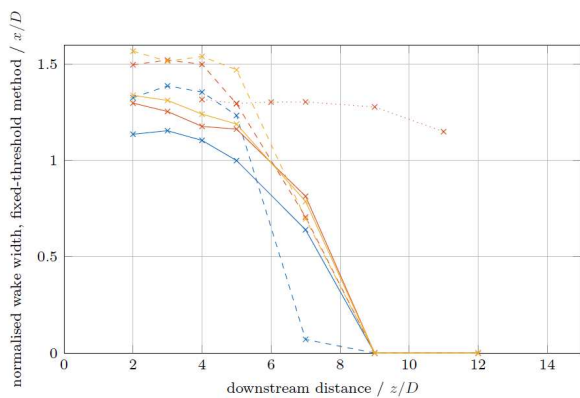
786 Wake width results for the flume cases following the maximum shear approach are  
 787 presented in Figure 16c. It could be suggested that the case with the highest turbulence tends  
 788 to produce a wider wake, but beyond this, no clear trends are visible. The much longer wake  
 789 for the low TI case is due to the unusually small amount of mixing taking place, and whilst  
 790 interesting for gaining insights into the mechanics of wake mixing, is of little relevance to  
 791 turbines in practical marine locations.



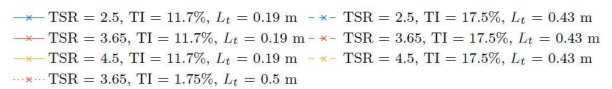
792 **a: fixed-threshold method.**



793 **b: full-width half-minimum method.**



794 **c: maximum-shear method**



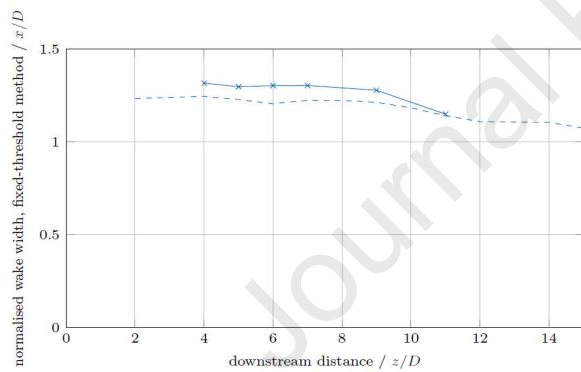
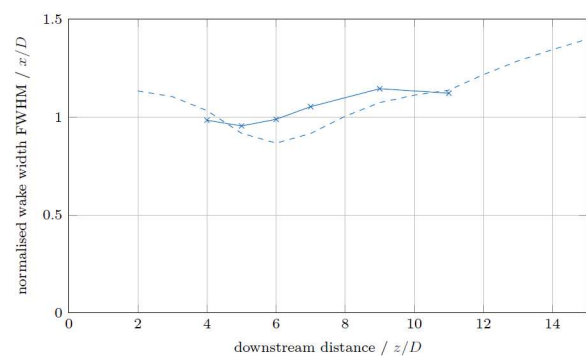
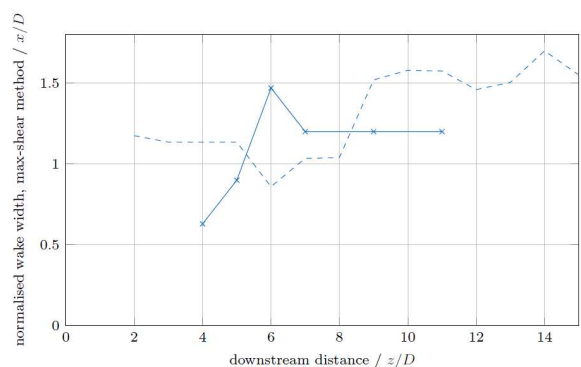
795 **Figure 16: Flume wake width**

796  
 810  
 811  
 812 **7.2 CFD**

813 Validation of the CFD against the low-turbulence flume tests can be seen for the fixed  
 814 threshold method, full-width half-minimum method and maximum-shear method in Figures  
 815 17. Validation of the CFD using the fixed-threshold method in Figure 17a, shows good  
 816 agreement between the CFD and the flume results, with both showing a slight narrowing of  
 817 the wake as it develops downstream, and only a slight under-prediction of wake width by the  
 818 CFD. A slight under-prediction of wake width by the CFD is also apparent in Figure 17b,  
 819 which compares CFD and flume results using the full-width half-minimum method. As with  
 820 the fixed-threshold method, there is good agreement with the trend of wake development, this  
 821 time with both methods showing a slight widening of the wake with downstream distance.  
 822 Agreement between the CFD and flume results using the maximum-shear method (Figure  
 823 17c) is less clear, although as mentioned in the discussion of Figure 16c, and further discussed  
 824 in section 7.3, results for the maximum-shear method suffer from convergence difficulties.  
 825 Nonetheless, both CFD and flume results indicate a slight widening for the wake with  
 826 increasing downstream distance, and CFD and flume results show a wake width of the same  
 827 order of magnitude. Agreement is not as good as with the fixed-threshold and full-width half-  
 828 minimum methods.

829 The flume and CFD results using the fixed-threshold method found that both sets of results  
 830 follow the same overall trends; starting with a near-wake width of 1.1 - 1.5D and staying  
 831 almost constant for 3 - 5D downstream, before narrowing. The CFD results show the same  
 832 trends with  $\lambda$  as the flume results. The CFD does though tend to under-predict the rate of  
 833 wake narrowing, with changes in the CFD predicted wake occurring 2 - 4D further  
 834 downstream than that seen in the flume.

835

836  
837840  
841  
842  
843  
844  
845  
846  
847  
848  
849  
850  
851840  
841  
842  
843  
844  
845  
846  
847  
848  
849  
850  
851838  
839840  
841  
842  
843  
844  
845  
846  
847  
848  
849  
850  
851

—x— TSR = 3.65, TI = 1.75%,  $L_t = 0.5$  m, flume  
 --- TSR = 3.65, TI = 0.96%,  $L_t = 0.8$  m, CFD

**Figure 17c** Validation of low-turbulence wake width

852

853 The flume and CFD results using the full-width half-minimum method found that initially  
 854 there is close agreement between the flume and CFD results in the near-wake, but that from  
 855 this point the results diverge, with the CFD results trending slightly wider than the flume  
 856 results. The trend with  $\lambda$  seen in the flume results is reproduced in the CFD results. Using the

857 full-width half-minimum method, the increase in wake width with downstream distance might  
 858 be expected, as the method gives an indication of the width of the region being in some way  
 859 affected by the wake, and this will tend to get wider as the wake mixes with the free-stream.  
 860 The reason for the flume results showing a narrowing with downstream distance is not  
 861 entirely clear, but if the wake profiles in Figure 10 are examined, then it can be seen that,  
 862 outside of the wake region, the profiles indicate an increased axial velocity, and show a slight  
 863 asymmetry and inhomogeneity in the flume outside of the immediate wake region. This will  
 864 affect the shapes of the profiles as well as making the choice of a reference velocity for  
 865 normalisation and calculation of deficit less clear, therefore affecting the width calculated  
 866 using the full-width half-minimum method. For the flume results the axial velocity used for  
 867 normalisation and deficit calculation is that which appears in Table 1, following measurement  
 868 of the centreline flow conditions in the flume at the point at which the turbine was placed.  
 869 CFD results were normalised and wake deficits calculated using the measured values for axial  
 870 velocity .

871 For the coarse grid wake widths calculated using the fixed-threshold method again showed  
 872 good agreement between the CFD and flume results. All wakes show an initial width of  
 873 between  $1 - 1.5D$ , which remains nearly constant until  $5 \leq z/D \leq 7$ , at which point they narrow  
 874 rapidly. For both flume and CFD results the initial wake width narrowing, and the rate of  
 875 narrowing are all well matched, as is the trend of an increasing wake width with  $\lambda$ .

876 Agreement between CFD and flume results for the fixed-threshold method appears to be  
 877 slightly better in the case of the coarse grid than for the fine grid. This is thought to be due to  
 878 the increase in mixing due to the higher TI conditions, and the inherent link between this  
 879 width metric and wake recovery. The turbulence in the coarse grid cases increases the mixing  
 880 and consequently the wake recovers very rapidly, with the 90% threshold being very quickly  
 881 achieved. This means that the wake widths very quickly drop to zero following this metric. A  
 882 more gradual wake recovery means there is less rapid mixing in the fine grid cases.

883 As with the full-width half-minimum results for the fine grid case, the flume and CFD  
 884 results for the coarse grid show good agreement in the near-wake region, before diverging,  
 885 with the flume results indicating a narrowing of the wake, whilst the CFD results indicate a  
 886 widening of the wake. Again, examination of Figure 10 indicates that there is some asymmetry  
 887 and inhomogeneity in the flume (due to the presence of the grid), and this will tend to distort  
 888 the shape of the profiles, and affect the width calculated using the full-width half-minimum  
 889 method.

890 Agreement, for all cases of turbulence and operating conditions, is only reasonable at best  
 891 when using the maximum-shear method. There is a general indication that higher-thrust cases  
 892 yield a wider wake as expected, however, the lack of convergence using this method means  
 893 that there is no clear trend in the far wake.

894

### 895 **7.3 Evaluation of different width metrics**

896 Three different wake width measurement metrics have been applied in this paper:

- 897 1. the fixed-threshold method,
- 898 2. the full-width half-minimum method, and
- 899 3. the maximum-shear method.

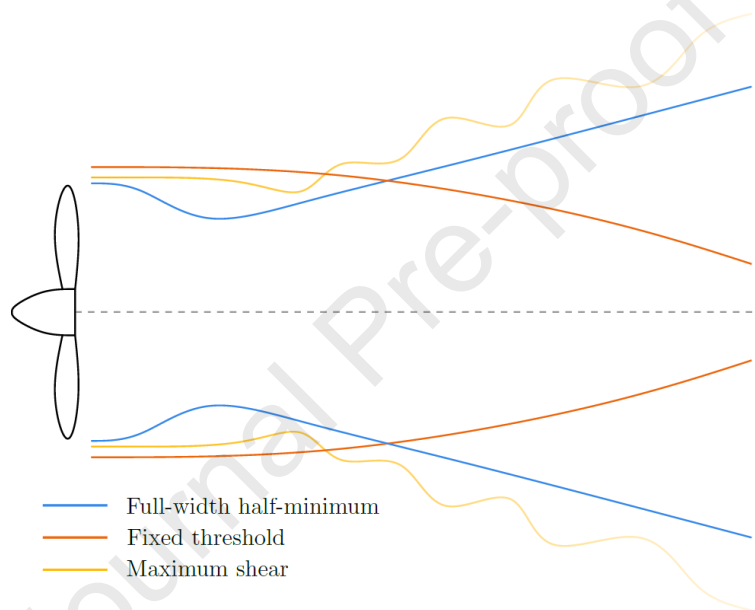
900 As the wake width can be difficult to define, these three metrics were applied as they each  
 901 provide a slightly different insight into the wake behaviour. The fixed-threshold method  
 902 yields the width of the region strongly impacted by the wake. In this work, the threshold was  
 903 chosen to be 90% wake recovery, which in conditions of high ambient TI meant that the wake  
 904 width reduces to zero within the region studied (i.e.  $z/D \leq 15$ ). By contrast, the full-width  
 905 half-minimum method applies a threshold, but calculates that threshold based on the

906 maximum deficit at that downstream distance. Consequently, this method provides a value for  
907 wake width which is related to the total width of the region impacted by the wake (i.e. the  
908 region where the velocity has been changed due to the presence of the turbine). It may be seen  
909 as a measure of the extent to which the wake has extended out into the flow region  
910 surrounding that directly downstream of the turbine. Applying both the fixed-threshold and  
911 full-width half-minimum methods allows an assessment to be made of how the wake is  
912 developing/recovering; for example, it might be found that the full-width half-minimum  
913 method indicates a widening of the wake, whilst the fixed-threshold method indicates a  
914 narrowing of the wake. This would indicate that the width of the region affected at all by the  
915 wake is increasing, but that this impact grows weaker as downstream distance increases.

916 The maximum-shear method does not try to define the wake width in terms of regions of  
917 greater or lesser impact, but rather uses the velocity shear to attempt to define the mid-point  
918 between the wake region and the free-stream. It is useful in as much as it defines a point  
919 within the flow, but as the wake develops and width of the shear layer between the wake and  
920 free-stream increases, the shapes of the wake profiles also change, and this definition of a  
921 point between the wake and free-stream regions becomes less useful as a comparison metric  
922 between wake profiles of different shapes. This is, in part, because this method as applied in  
923 this paper only accounts for the position of the point of maximum shear but pays no regard to  
924 the strength of the shear. In addition, when applying these three methods it was found that  
925 they respond differently to wake profiles of different shapes. In particular, the maximum  
926 shear method showed itself to be particularly sensitive to slight changes in the mean flow-  
927 field when the wake profiles were approximately v-shaped. The three methods have been  
928 applied to the low turbulence CFD case,  $\lambda = 3.65$ . Each of the metrics has been applied to the  
929 same velocity data, so any difference in the rates of convergence are due to sensitivity  
930 inherent in the metrics themselves, rather than a lack of convergence in the velocity data. For  
931 reference, wake velocity profiles for this run can be seen in Figure 9. The reader will notice  
932 some slight asymmetry in the wake. This is thought to be due to the asymmetry in the  
933 experimental setup (and CFD). The walls and floor of the flume were modelled as no-slip  
934 boundaries, whereas the upper domain boundary was set to a zero-shear condition.

935 As the wake develops with downstream distance, the shape of the velocity profiles changes  
936 from one with very steep sides (shaped approximately like an inverted top-hat) to profiles  
937 which are v-shaped, with an almost linear change in velocity with cross-stream position, and  
938 therefore an almost uniform velocity shear from near the centre to the very edge of the wake.  
939 This transition is a gradual one, but by approximately  $z/D = 6$ , the profiles have become  
940 distinctly v-shaped. For the inverted top-hat profiles, their steep-sides mean that the point of  
941 maximum-shear is located within a relatively small cross-stream extent. Any small changes in  
942 the mean flow field have little impact on the cross-stream position of the point of maximum-  
943 shear, and therefore the value of wake width in this region converges quickly. In contrast to  
944 this, for v-shaped wake profiles the almost linear change in velocity with cross-stream  
945 position means that there is a large cross-stream extent with an almost identical amount of  
946 velocity shear, the value of which is approximately the same as that of the maximum-shear.  
947 The result of this is that any small changes to the mean velocity field (and therefore the wake  
948 profiles) can cause the position of maximum-shear to move from nearly the centreline to the  
949 very edge of the wake, despite there being no significant change to the wake profile itself.  
950 This means that the wake width based on the point of maximum-shear can vary greatly, and  
951 the metric is very sensitive to slight changes in the velocity profiles. A schematic comparing  
952 the three different metrics is presented in Figure 18. This comparison varies depending on the  
953 precise tip-speed ratio and inlet flow conditions; the representation here is based on the  
954 behaviour for tip-speed ratios around the point of maximum  $C_P$  for low turbulence conditions  
955 and is intended to show the general behaviour of the metrics, but is not intended to be to-

956 scale. All three metrics initially have a similar width, slightly larger than the turbine diameter.  
 957 The width measured using the fixed-threshold method tends to decrease as mixing takes place  
 958 and the wake recovers. In contrast to this, the full-width half-minimum method initially shows  
 959 a decrease in width as the wake velocity profile changes from an inverted top-hat shape to a v-  
 960 shape, before showing a steady increase as the mixing region between the wake and the free-  
 961 stream spreads outwards. A similar trend occurs with the maximum-shear method, which  
 962 initially exhibits a nearly constant width (due to the inverted top-hat shape of the wake  
 963 velocity profiles). As the wake profiles become more v-shaped, the maximum-shear method  
 964 starts to demonstrate convergence issues, and only a general trend of increasing width can be  
 965 identified. This is represented in this schematic by the movement and fading of the line  
 966 representing this metric. Comparing Figure 18 to Figure 1, it can be seen that the fixed-  
 967 threshold method behaves in a similar way to the inner edge of the shear layer (between the  
 968 shear layer itself and the wake core), whereas the full-width half-minimum method comes  
 969 closer to representing the general expansion of the wake into the free-stream region.



970 **Figure 18** Schematic (not to scale) comparing the general behaviour of the three different  
 971 wake measurement metrics.  
 972

973 The maximum-shear method always gives a wake 'edge' within the shear layer, but as the  
 974 shear layer increases in thickness and the wake velocity profiles become v-shaped, this could  
 975 be anywhere from the boundary between the shear layer and core region to the boundary  
 976 between the shear layer and free-stream, which leads to this metric's poor convergence. The  
 977 maximum-shear method only gives reliably converged results in the near wake, where the  
 978 shear layer between wake core and free-stream is thin and distinct.

979 Given that the maximum-shear method shows convergence difficulties for v-shaped  
 980 profiles which appear both in CFD results and the fact that the fixed-threshold and full-width  
 981 half-minimum methods provide information with direct applicability to array designers, it is  
 982 suggested that the maximum-shear method is of limited value in the discussion of wake  
 983 width.

984

## 985 **7.4 Impact of turbulence on wake width**

### 986 **7.4.1 Turbulence intensity**

987 The impact of TI on wake width is explored using the fixed threshold, full-width half-  
 988 minimum and maximum-shear methods.

1089 The fixed-threshold metric shows that, regardless of ambient TI, all wakes initially have  
 1090 very similar widths. These start to diverge from approximately  $z/D=5$  downstream, with the  
 1091 cases with higher TI showing a more rapid narrowing than those with lower TI. This is due to  
 1092 the increased levels of mixing encouraged by the higher turbulence intensities. The fixed-  
 1093 threshold method provides an indication of the width of the region strongly affected by the  
 1094 presence of the turbine; more mixing and faster wake recovery means that the region of the  
 1095 highest velocity deficit will reduce more rapidly, narrowing the wake by this metric.

1096 The full-width half-minimum metric shows a general steady increase in wake width for all  
 1097 TI cases, whilst showing that the higher TI cases yield a wider wake. This can again be  
 1098 explained by the increased levels of mixing from the higher TI ambient flow. The full-width  
 1099 half-minimum method gives an indication of the width of the region impacted at all by the  
 1000 wake; increased mixing between the wake and free-stream leads to a faster transfer of  
 1001 momentum to the wake region from the free-stream (leading to faster wake recovery), but also  
 1002 means that the effect of the velocity deficit in the wake region will be moved further and  
 1003 faster into the free-stream. This leads to a greater width being affected to some extent by the  
 1004 wake in the higher TI cases, whilst simultaneously reducing the width of the region strongly  
 1005 affected by the wake.

1006 The maximum-shear method also indicates a dependence of wake width on TI, with the  
 1007 higher turbulence cases there is a trend to increasing wake width. This gives some  
 1008 information about the shape of the wake recovery profiles and suggests that they become  
 1009 flatter with slightly steeper sides as TI increases. Another way to see this is that the wakes  
 1010 become more homogeneous with increased TI, reflected in the increased centreline velocity  
 1011 recovery (Figure 14a). As discussed, choosing to define the point of maximum-shear in the  
 1012 wake as the 'edge' of the wake, has less meaning than the fixed-threshold and full-width half-  
 1013 minimum methods, which either give the region strongly affected by the wake, or the region  
 1014 affected to some extent, and, whilst it is interesting to see a dependence of the maximum-  
 1015 shear method on TI, it does not give any real insight for array designers.

1016 Overall, it can be said that an increase in ambient TI has an impact on the width of the  
 1017 wake of a tidal stream turbine. The increase in mixing associated with the increase in TI  
 1018 means that the width of the region of highest velocity deficit reduces more rapidly, whilst at  
 1019 the same time, the overall wake width increases (albeit with its impact weakened). This result  
 1020 will be important for array designers and suggests that, combined with the results for velocity  
 1021 recovery, arrays in areas of higher ambient TI may benefit from a reduced longitudinal  
 1022 spacing, and increased lateral spacing. In effect, higher TIs tend to shorten and widen wakes.

#### 1024 7.4.2 Turbulence length scale

1025 The impact of turbulence length scale on wake width is examined using the fixed  
 1026 threshold, full-width half-minimum and maximum-shear methods. The fixed threshold  
 1027 method shows that the width in the case with medium  $L_t$  (0.78 m) remains fairly constant,  
 1028 whereas that with the shortest  $L_t$  (0.45 m) shows the widest initial width with rapid narrowing.

1029 The case with the longest  $L_t$  (1.5 m) shows a similar trend to that of the shortest  $L_t$ , albeit  
 1030 with a less rapid narrowing. There is, however, no clear overall trend of wake width with  
 1031 length scale using this method. The full-width half-minimum method resulted in the mid-  
 1032 wake region ( $3 \leq z/D \leq 11$ ) with the shortest  $L_t$  having the widest wake, whilst the longest  $L_t$   
 1033 shows the narrowest. From  $z/D \sim 11$ , the longest length scale, then results in the widest width.  
 1034 This could suggest that the largest turbulence length scales demonstrate less initial mixing  
 1035 (and therefore the narrow wake in the mid-wake region), but a more thorough mixing in the  
 1036 far wake region. Similar behaviour is also found when the maximum-shear method is applied.

1037 Overall, there is no clear trend of impact of  $L_t$  on wake width, regardless of which metric is  
 1038 used. However, only three different length scales have been compared here, and it has not

1039 been possible to completely isolate the effects of TI and length scale. It might also be the case  
 1040 that turbulent length scales smaller or larger than those used here could have a different  
 1041 impact and would be worthy of further investigation to establish any possible impact.

1042

### 1043 **7.5 Impact of tip-speed ratio on wake width**

1044 Regardless of which metric is used, there is a clear trend in the data that an increase in  $\lambda$   
 1045 results in a wider wake. This trend is clearest when the fixed-threshold method is used. Here,  
 1046 all wakes maintain their initial width or widen slightly, before tending to narrow with  
 1047 downstream distance. All the wakes show the same general trends, but with the lowest thrust  
 1048 cases in general being the narrowest. The differences in width are most apparent for the low  $\lambda$   
 1049 values, whilst the higher  $\lambda$  values are more closely grouped together. This corresponds well to  
 1050 the thrust curve. The same overall trend was found in wake widths calculated using the full-  
 1051 width half-minimum method. As with the fixed-threshold method, the cases where the turbine  
 1052 is operating at a higher thrust demonstrate a greater wake width. However, with the full-width  
 1053 half minimum method, the overall trend is that the wake width steadily increases with  
 1054 downstream distance. This difference, when compared to the fixed-threshold method, is due  
 1055 to firstly, the way that the two methods respond to wake profiles of different shapes, and  
 1056 secondly, as the full-width half-minimum method is a measure of the width of the region  
 1057 impact to some extent by the wake, this can be expected to increase as the wake spreads out  
 1058 downstream, even if its strength diminishes. The cases closest to peak power, with  $3.0 \leq \lambda \leq$   
 1059  $4.5$  initially show a reduction in wake width until  $z/D \sim 6$  downstream of the rotor, after  
 1060 which they steadily increase in width.  $\lambda \geq 3.65$  all show the same initial width, with the  $\lambda =$   
 1061  $3.0$  case showing a similar initial width as well. All of these cases show a profile with very  
 1062 steep sides, similar to an inverted 'top-hat' shape, in the near wake. These steep sides are only  
 1063 slightly wider than the turbine and are in the same position regardless of the velocity deficit in  
 1064 this region. Applying the full-width half-minimum method to an inverted top-hat shape will  
 1065 give an almost identical result for wake width, regardless of the maximum velocity deficit.  
 1066 This leads to the near-wake width of each of these cases being nearly identical. In contrast,  
 1067 the low thrust cases with tip-speed ratios of  $\lambda = 1.5$  and  $2.5$  do not show these inverted top-hat  
 1068 profiles but show v-shaped profiles instead. As these v-shaped velocity profiles develop  
 1069 downstream, they reduce in depth and become proportionally wider, which is reflected in the  
 1070 steady increase in width measured using the full-width half minimum method. For the cases  
 1071 where the initial profile is that of an inverse top-hat, as the wake develops and mixes with the  
 1072 free-stream this inverse top-hat first becomes U-shaped, then v-shaped (leading to the  
 1073 apparent decrease in wake width), from which point the profiles reduce in depth and become  
 1074 proportionally wider, matching the trend shown with the low-thrust cases. These profiles, for  
 1075 different  $\lambda$  values, can be seen in Figures 9. It is interesting to note that the  $\lambda$  values for which  
 1076 the reduction in wake width is greatest are around the point of maximum  $C_p$ .

1077 Trends in wake width with  $\lambda$  are still apparent when the maximum shear method is used,  
 1078 however, due to the convergence difficulties associated with this method, the differences are  
 1079 less clear. There are two distinct regions:  $z/D < 5$  and  $z/D > 5$ . The reason for this is again the  
 1080 wake shape, being either an inverted top-hat, or approximately v-shaped.  $\lambda \geq 3.0$  exhibit the  
 1081 inverted top-hat profile until  $z/D \sim 5$ , hence the width using the maximum-shear method is  
 1082 well defined. Beyond this point, the profiles become v-shaped; this means there is a large  
 1083 cross-stream extent with an almost identical amount of shear, which itself is approximately  
 1084 the maximum-shear in the wake. Any slight changes in the profiles can radically change the  
 1085 measured width, explaining the fluctuations visible in the region  $z/D > 5$ .

1086 All three metrics demonstrate a clear impact of tip-speed ratio on wake width, with the  
 1087 high  $\lambda$  values, high thrust cases demonstrating a wider wake. An increase in width with  
 1088 increasing turbine thrust can be explained by the increase in resistance to the flow causing

1089 more of the flow to be divert outwards and around the swept area of the turbine, creating a  
1090 wider wake.

## 1091 **7.6 CFD**

1092 The low-turbulence flume tests found that the CFD overpredicts TI in the near wake  
1093 region. However, from  $z/D=9$  to the end of the available flume data the agreement is very  
1094 good, and an extrapolation of the results from the flume would show good agreement with the  
1095 CFD from this point onwards, suggesting that the CFD accurately reproduces the wake by this  
1096 point. Part of the reason for the over prediction of TI in the near wake will be down to the  
1097 CFD's slight under-prediction of velocity recovery in this region (Figure 11a), meaning that  
1098 the same magnitude of fluctuations would yield a higher value of TI. However, this is not  
1099 enough to completely explain the difference. The poor agreement in the near-wake may be  
1100 improved by further increasing the mesh density, or by further investigation into possible flow  
1101 separation as the blade boundary layer transitions from being laminar to being turbulent.

1102 Good agreement between flume and CFD from  $z/D \sim 4$  onwards was found using the fine  
1103 grid. The CFD does reproduce the trend in the near-wake of the flume results and a  
1104 dependence of TI on  $\lambda$ . Further upstream, the CFD tends to overpredict the TI. The CFD  
1105 reproduces both the trend of lower  $\lambda$  values producing the highest initial TI, but also that any  
1106 difference between these cases becomes indistinguishable from  $z/D \sim 4$ .

1107 Good agreement was also found between flume and CFD using the coarse grid throughout  
1108 the region. However, neither the flume data nor the CFD results demonstrated a dependence  
1109 of wake TI on  $\lambda$ .

1110 Centreline wake  $L_t$  has been validated using data from the low-turbulence flume test. As  
1111 for the TI the CFD tends to overpredict  $L_t$  in the near- and mid-wake regions, but agreement is  
1112 good from  $z/D \sim 9$  onwards. As with TI, it is thought that the poor agreement in the near-  
1113 wake may be improved by increasing mesh density in the region surrounding the turbine.

1114 The CFD results for the fine grid, for  $\lambda = 2.5$  and  $\lambda = 3.65$ , reflect the trend in the flume  
1115 results of a gradual rise in  $L_t$  as the wake develops, but show an under-prediction in the rate of  
1116 increase. Larger changes in  $\lambda = 4.5$  indicate a possible convergence issue; other studies have  
1117 shown that a sample time of 50 s is at the lower bound of what is required to obtain reliable  
1118 well converged results for a higher order statistic such as integral length scale, in flows of this  
1119 nature using a sample rate similar to the 200 Hz used in this study [46]. As the smallest time  
1120 scales were typically approximately 0.2 s, a sample rate of 200 Hz was more than adequate to  
1121 accurately capture these fluctuations.

1122 The CFD results for the coarse grid for the three  $\lambda$  values modelled show similar values, in  
1123 the wake, of  $L_t \sim 0.25$  m, which remains nearly constant throughout the wake, in contrast to  
1124 the steady increase of  $L_t$  seen in the flume results. The agreement is good in the near-wake  
1125 region, but deteriorates as the wake develops, indicating a general trend in the CFD to under-  
1126 predict length scale. The value of  $L_t$  in the CFD models for the coarse grid cases is slightly  
1127 higher than those found in the fine grid cases, which reflects the trend between in the flume  
1128 results. More detailed explanations can be found in Ebdon [51].

1129

### 1130 **7.6.1 Impact of turbulence on wake turbulence characteristics**

#### 1131 **7.6.1.1 Turbulence intensity**

1132 The impact of ambient TI on wake centreline TI was analysed using four CFD cases. The  
1133 results indicated a possible weak dependence of wake TI on ambient TI, with a higher  
1134 ambient TI leading to a higher wake TI. This agrees with the mild dependence on ambient TI  
1135 found in the flume results. The largest difference between the cases was in the near- to mid-  
1136 wake region; by  $z/D=10$ , there is little difference in the centreline turbulence intensities,  
1137 regardless of the ambient TI upstream.

1138 In general, there is little difference between the cases, with all cases showing a slight  
 1139 increase in length scale with increasing downstream distance. Both the trends in, and the  
 1140 magnitudes of  $L_t$ , are similar for all cases, indicating that ambient TI has little dependence on  
 1141 wake  $L_t$ .

#### 1142 **7.6.1.2 Turbulence length scale**

1143 The ambient  $L_t$  on wake centreline TI was assessed through three CFD runs with identical  
 1144  $\lambda$  values, similar TIs, but differing  $L_t$  values. No clear trend was observed, although it could  
 1145 be said that the cases with the shortest and longest values of ambient  $L_t$  show similar  
 1146 behaviours, with the medium  $L_t$  showing a significantly lower initial TI. This could indicate a  
 1147 non-linear response of wake centreline TI to  $L_t$ , for example suggesting that wake mixing  
 1148 might not simply increase or decrease with increasing ambient  $L_t$ , but rather that there might  
 1149 be a value of ambient  $L_t$  which causes most mixing, and a longer or shorter  $L_t$  leads to  
 1150 reduced wake mixing.

1151 The effect of ambient  $L_t$  was that in all cases a sharp initial rise in  $L_t$  was found followed  
 1152 by a reduction, before resuming a steady rise towards the far wake. All cases show similar  
 1153 results beyond approximately  $z/D=10$ . Here there appears to be some dependence of wake  $L_t$   
 1154 on ambient  $L_t$ . Possibly a larger ambient  $L_t$  leads to a larger value of  $L_t$  in the near- to mid-  
 1155 wake, but it also seems to cause the point at which  $L_t$  peaks before reducing to move further  
 1156 downstream.

#### 1157 **7.7 Impact of tip-speed ratio on wake turbulence characteristics**

1158 The impact of  $\lambda$  on centreline TI was examined via seven different CFD cases in a low-  
 1159 turbulence environment of approximately 1.5%. The lowest  $\lambda$  values ( $\lambda = 1.5$  and  $\lambda = 2.5$ )  
 1160 initially demonstrated a very high initial TI, which very quickly drops.  $\lambda$  values around the  
 1161 point of peak CP ( $\lambda = 3.65$ ; 4.0; 4.5) start at approximately 25% at  $z/D=2$ , rising to  
 1162 approximately 30% at  $z/D=5$ , before reducing as the downstream distance increases further.  
 1163 This initial increase in TI followed by a decrease has been observed in studies such as that by  
 1164 Maganga et al. [13] and Baba-Ahmadi and Dong [57], and is thought to be due to the shear  
 1165 layers from either side of the wake merging in the centre. The high initial  $L_t$  for the lowest  
 1166 values of  $\lambda$  may be due to blade stalling changing the characteristics of the turbulence in these  
 1167 cases; two  $\lambda$  values are within or close to the stall region. The initial high TI followed by a  
 1168 rapid reduction in the  $\lambda = 1.5$  case may be related to the rapid centreline wake recovery in this  
 1169 case: a higher level of turbulence promoting more rapid mixing and wake recovery

1170 For array designers concerned with the placement of turbines, the region of increased TI in  
 1171 the near wake will be of some interest, however it is unlikely to be of great relevance if the  
 1172 turbines are to have a longitudinal spacing of more than approximately  $z/D=8$ , or even  
 1173 possibly less in conditions of higher ambient turbulence. Perhaps of more interest would be  
 1174 that, from  $z/D \sim 10$ ,  $\lambda$  (and therefore turbine operating condition) has little impact on wake TI.

1175 The centreline turbulence length scale,  $L_t$ , for each of the  $\lambda$  values, used in the low-  
 1176 turbulence CFD case, generally displayed a gradual increase value as the wake develops. This  
 1177 is consistent with that seen in the flume results and is due to the smaller length scales  
 1178 dissipating due to viscous forces, leaving larger length scales dominant. However, there is a  
 1179 significant difference between the cases in their initial behaviour, with some cases showing an  
 1180 initial increase in  $L_t$ , followed by a comparable decrease, before gradually increasing once  
 1181 more. This complex behaviour initially appears to be linked to  $C_p$ , as tip-speed ratios with  
 1182 higher values of  $C_p$  appear to show a larger initial increase than those with a lower value of  
 1183  $C_p$ . However, the representative length scales of the dominant turbulent features might be  
 1184 dependent on the rotational frequency of the turbine, rather than the operational condition (i.e.  
 1185 where it is operating on the curves of  $C_p$ ,  $C_T$  and  $C_\theta$ ). The ambient  $L_t$  in these cases is  
 1186 approximately 0.8 m, meaning that  $L_t$  downstream of the turbine is much smaller than

1187 upstream of it. The presence of the turbine leads to a reduction in length scale, which may be  
 1188 caused by large turbulent features being broken up by their passage through the rotating  
 1189 turbine blades. The greater the rotational frequency, the smaller the resultant turbulent  
 1190 features, explaining why higher  $\lambda$  values have a smaller initial length scale. The exceptions to  
 1191 this,  $\lambda = 1.5$  and  $\lambda = 2.5$ , may not fit this pattern due to the blade-stall effects discussed above.  
 1192 A stalled blade can be expected to produce turbulence with different characteristics to that of  
 1193 an unstalled blade, with effects such as flow separation leading to higher wake TI, which  
 1194 could explain the differences between these two cases. This more complex behaviour is only  
 1195 apparent in the near wake, however; from  $z/D \sim 10$ , the length scales become similar  
 1196 regardless of  $\lambda$ , suggesting that it need not be considered for array layouts for  $z/D \geq 10$ .

1197  
 1198  
 1199

## 1200 **8 CONCLUSIONS**

### 1201 **Impact of turbulence on:**

#### 1202 • ***Performance***

1203 For all tip-speed ratios, an increase in turbine characteristics and magnitude of fluctuations  
 1204 is seen at higher turbulence intensities. Turbulence length scale seems to have little impact.

#### 1205 • ***Wakes***

1206 Turbulence intensity was found to strongly impact wake recovery, both centreline and  
 1207 volumetric averaged velocity. An increase in TI always led to increased recovery, there is  
 1208 some suggestion that, beyond the near wake, turbulence intensities above 10% have similar  
 1209 results.

1210 Turbulence intensity has an impact on wake width. An increase in TI causes the fixed-  
 1211 threshold width to narrow, but the full-width half-minimum and maximum-shear widths to  
 1212 widen. Taken together, this indicates that the overall wake width is increasing, but that the  
 1213 region strongly impacted by the wake is decreasing. Finally, turbulence length scale was not  
 1214 found to have a strong impact on turbine wakes.

#### 1215 **Wake width metrics**

1216 The fixed-threshold and full-width half-minimum methods were found to be less sensitive  
 1217 to wake shape than the maximum shear method, with each providing subtly different  
 1218 information about the wake. Due to the way these metrics complement each other, providing a  
 1219 more complete picture of the nature of the wake when used together, the authors recommend  
 1220 that both are used in future studies.

#### 1221 **The impact of operating condition on wakes**

1222 Turbine operating condition strongly impacts the wakes of tidal turbines, although with the  
 1223 exception of the impact on wake width, these differences become small by  $\sim z/D = 10$ .

1224 The turbine operating condition has been shown to have an impact on wake width, with  
 1225 wider wakes occurring as turbine thrust increases. This impact can be seen throughout the  
 1226 wake length.

#### 1227 **Implications for tidal turbine arrays**

1228 The ambient TI of a site must be taken into account for the placement of turbines in an  
 1229 array.

1230 The relationship between TI and wake recovery and wake width suggests that, for an array  
 1231 site with higher ambient TI, longitudinal spacing may be reduced, while lateral spacing may  
 1232 need to be increased due to the widening of the overall area affected by the wakes.

1233 Arrays of turbines designed to maintain rated power through overspeed will require a  
 1234 greater lateral spacing as both the overall width of the region affected by the wake, as well as  
 1235 the width of the region most heavily impacted, increase with greater  $C_T$ .

### 1236 Acknowledgements

1237 The authors acknowledge the financial support provided by:

- 1238 • The Welsh Government and Higher Education Funding Council for Wales through the Sêr  
 1239 Cymru National Research Network for Low Carbon, Energy and the Environment.
- 1240 • EPSRC EP/N020782/1, Dynamic Loading on Turbines in a tidal array (DyLoTTA).
- 1241 • Access to IFREMER flume was funded through an EPSRC IAA and IFREMER. The  
 1242 authors would like to thank the staff at IFREMER for their expertise and support during  
 1243 the testing.
- 1244 • The supercomputing facilities at Cardiff University operated by Advanced Research  
 1245 Computing at Cardiff (ARCCA) on behalf of the Cardiff Supercomputing Facility and the  
 1246 HPC Wales and Supercomputing Wales (SCW) projects. The latter is part-funded by the  
 1247 European Regional Development Fund (ERDF) via the Welsh Government.

1248

### 1249 References

- 1250 1 G. Pinon, P. Mycek, G. Germain, and E. Rivoalen, "Numerical simulation of the wake of marine  
 1251 current turbines with a particle method," *Renewable Energy*, vol. 46, pp. 111 – 126, 2012.
- 1252 2 Lewis, M., Neill, S.P., Robins, P., Hashemi, M.R. and Ward, S. "Characteristics of the velocity  
 1253 profile at tidal-stream energy sites." *Renewable Energy*, 114, pp.258-272, 2017.
- 1254 3 Togneri, M., Lewis, M., Neill, S. and Masters, I. " Comparison of ADCP observations and 3D  
 1255 model simulations of turbulence at a tidal energy site." *Renewable Energy*, 114, pp.273-282,  
 1256 2017.
- 1257 4 Lewis, M., McNaughton, J., Márquez-Dominguez, C., Todeschini, G., Togneri, M., Masters, I.,  
 1258 Allmark, M., Stallard, T., Neill, S., Goward-Brown, A. and Robins, P. "Power variability of tidal-  
 1259 stream energy and implications for electricity supply." *Energy*, 183, pp.1061-1074, 2019.
- 1260 5 C. H. Frost, P. S. Evans, M. J. Harrold, A. Mason-Jones, T. O'Doherty and D. M. O'Doherty,  
 1261 "The impact of axial flow misalignment on a tidal turbine," *Renewable Energy*, vol. 113, pp. 1333  
 1262 - 1344, 2017.
- 1263 6 A. Mason-Jones, Performance assessment of a Horizontal Axis Tidal Turbine in a high velocity  
 1264 shear environment. PhD thesis, School of Engineering, Cardiff University, 2010.
- 1265 7 Y. Zhang, J. Zhang, Y. Zheng, C. Yang, W. Zang, and E. Fernandez Rodriguez, "Experimental  
 1266 Analysis and Evaluation of the Numerical Prediction of Wake Characteristics of Tidal Stream  
 1267 Turbine," *Energies*, vol. 10:2057, 2017.
- 1268 8 P. Lissaman, "Energy effectiveness of arbitrary arrays of wind turbines," *J. Energy*, vol. 3, no. 6,  
 1269 pp. 323–328, 1979.
- 1270 9 N. Jensen, "A note on wind generator interaction," tech. rep., Risø National Laboratory,  
 1271 Denmark, 1983.
- 1272 10 S. Frandsen, R. Barthelmie, S. Pryor, O. Rathmann, S. Larsen, J. Højstrup, and M. Thøgersen,  
 1273 "Analytical modelling of wind speed deficit in large offshore wind farms," *Wind Energy*, vol. 9,  
 1274 no. 1-2, pp. 39– 53, 2006.
- 1275 11 M. Bastankhah and F. Porté-Agel, "A new analytical model for wind turbine wakes," *Renewable*  
 1276 *Energy*, vol. 70, pp. 116 – 123, 2014. Special issue on aerodynamics of offshore wind energy  
 1277 systems and wakes.
- 1278 12 W.-H. Lam and L. Chen, "Equations used to predict the velocity distribution within a wake from  
 1279 a horizontal-axis tidal-current turbine," *Ocean Engineering*, vol. 79, pp. 35–42, 2014.

- 1280 13 F. Maganga, G. Germain, J. King, G. Pinon, and E. Rivoalen, "Experimental characterisation of  
1281 flow effects on marine current turbine behaviour and on its wake properties," *IET Renewable*  
1282 *Power Generation*, vol. 4, pp. 498–509, November 2010.
- 1283 14 W.-H. Lam, L. Chen, and R. Hashim, "Analytical wake model of tidal current turbine," *Energy*,  
1284 vol. 79, pp. 512 – 521, 2015.
- 1285 15 P. Mycek, G. Germain, B. Gaurier, G. Pinon, E. Rivoalen, "Numerical and experimental study of  
1286 the interaction between two marine current turbines" *International Journal of Marine Energy*,  
1287 Vol. 1, pp 70-83, 2013
- 1288 16 M. E. Harrison, W. M. J. Batten, L. E. Myers, and A. S. Bahaj, "Comparison between CFD  
1289 simulations and experiments for predicting the far wake of horizontal axis tidal turbines," *IET*  
1290 *Renewable Power Generation*, vol. 4, pp. 613–627, November 2010.
- 1291 17 R. Malki, A. Williams, T. Croft, M. Togneri, and I. Masters, "A coupled blade element  
1292 momentum – Computational fluid dynamics model for evaluating tidal stream turbine  
1293 performance," *Applied Mathematical Modelling*, vol. 37, pp. 3006–3020, 2013.
- 1294 18 G. Bai, J. Li, P. Fan, and G. Li, "Numerical investigations of the effects of different arrays on  
1295 power extractions of horizontal axis current turbines," *Renewable Energy*, vol. 53, pp. 180–186,  
1296 2013.
- 1297 19 T. Nishino and R. H. Willden, "Effects of 3-D channel blockage and turbulent wake mixing on  
1298 the limit of power extraction by tidal turbines," *International Journal of Heat and Fluid Flow*,  
1299 vol. 37, pp. 123–135, 2012.
- 1300 20 A. Bahaj and L. Myers, "Shaping array design of marine current energy converters through scaled  
1301 experimental analysis," *Energy*, vol. 59, pp. 83– 94, 2013.
- 1302 21 P. Mycek, B. Gaurier, G. Germain, G. Pinon, and E. Rivoalen, "Experimental study of the  
1303 turbulence intensity effects on marine current turbines behaviour. part I: One single turbine,"  
1304 *Renewable Energy*, vol. 66, pp. 729–746, 2014.
- 1305 22 B. Morandi, F. D. Felice, M. Costanzo, G. Romano, D. Dhom'è, and J. Allo, "Experimental  
1306 investigation of the near wake of a horizontal axis tidal current turbine," *International Journal of*  
1307 *Marine Energy*, vol. 14, pp. 229–247, 2016.
- 1308 23 S. Tedds, I. Owen, and R. Poole, "Near-wake characteristics of a model horizontal axis tidal  
1309 stream turbine," *Renewable Energy*, vol. 63, pp. 222– 235, 2014.
- 1310 24 J. Schluntz and R. Willden, "The effect of blockage on tidal turbine rotor design and  
1311 performance," *Renewable Energy*, vol. 81, pp. 432–441, 2015.
- 1312 25 S. R. Turnock, A. B. Phillips, J. Banks, and R. Nicholls-Lee, "Modelling tidal current turbine  
1313 wakes using a coupled RANS-BEMT approach as a tool for analysing power capture of arrays of  
1314 turbines," *Ocean Engineering*, vol. 38, pp. 1300–1307, 2011.
- 1315 26 R. Malki, I. Masters, A. J. Williams, and T. N. Croft, "Planning tidal stream turbine array layouts  
1316 using a coupled blade element momentum computational fluid dynamics model," *Renewable*  
1317 *Energy*, vol. 63, pp. 46– 54, 2014.
- 1318 27 D. O'Doherty, A. Mason-Jones, C. Morris, T. O'Doherty, C. Byrne, P. Prickett, and R.  
1319 Grosvenor, "Interaction of marine turbines in close proximity," in *Proc. of 9th European Wave*  
1320 *and Tidal Energy Conference (EWTEC), Southampton, UK, 2011.*
- 1321 28 T. Stallard, R. Collings, T. Feng, and J. Whelan, "Interactions between tidal turbine wakes:  
1322 experimental study of a group of three-bladed rotors," *Philosophical Transactions of the Royal*  
1323 *Society of London A: Mathematical, Physical and Engineering Sciences*, vol. 371, no. 1985,  
1324 2013.
- 1325 29 M. Nuernberg and L. Tao, "Experimental study of wake characteristics in tidal turbine arrays,"  
1326 *Renewable Energy*, vol. 127, pp. 168–181, 2018.
- 1327 30 P. Jeffcoate, T. Whittaker, C. Boake, and B. Elsaesser, "Field tests of multiple 1/10 scale tidal  
1328 turbines in steady flows," *Renewable Energy*, vol. 87, pp. 240–252, 2016.

- 1329 31 C. Morris, D. O'Doherty, A. Mason-Jones, and T. O'Doherty, "Evaluation of the swirl  
1330 characteristics of a tidal stream turbine wake," *International Journal of Marine Energy*, vol. 14,  
1331 pp. 198–214, 2016.
- 1332 32 P. Mycek, B. Gaurier, G. Germain, G. Pinon, and E. Rivoalen, "Experimental study of the  
1333 turbulence intensity effects on marine current turbines behaviour. part II: Two interacting  
1334 turbines," *Renewable Energy*, vol. 68, pp. 876–892, 2014.
- 1335 33 I. Afgan, J. McNaughton, S. Rolfo, D. Apsley, T. Stallard, and P. Stansby, "Turbulent flow and  
1336 loading on a tidal stream turbine by LES and RANS," *International Journal of Heat and Fluid  
1337 Flow*, vol. 43, pp. 96–108, 2013.
- 1338 34 T. Blackmore, W. Batten, and A. Bahaj, "Influence of turbulence on the wake of a marine current  
1339 turbine simulator," *Proc. R. Soc. A*, vol. 470, p. 20140331, 2014.
- 1340 35 P. Ouro, M. Harrold, T. Stoesser, and P. Bromley, "Hydrodynamic loadings on a horizontal axis  
1341 tidal turbine prototype," *Journal of Fluids and Structures*, vol. 71, pp. 78–95, 2017.
- 1342 36 M. Churchfield, Y. Li, and P. Moriarty, "A large-eddy simulation study of wake propagation and  
1343 power production in an array of tidal-current turbines," *Phil. Trans. R Soc. A*, vol. 371, p.  
1344 20120421, 2013.
- 1345 37 C. Morris, *Influence of Solidity on the Performance, Swirl Characteristics, Wake Recovery and  
1346 Blade Deflection of a Horizontal Axis Tidal Turbine*. PhD thesis, School of Engineering, Cardiff  
1347 University, 2014.
- 1348 38 M. Ikhennecheu, G. Germain, P. Druault, B. Gaurier, "Experimental investigation of the turbulent  
1349 wake past realistic seabed elements for velocity variations characterization in the water column,"  
1350 *Renewable Energy*, 2020.
- 1351 39 P. Mercier, M. Ikhennecheu, P. Druault, S. Guilloux, G. Germain, "The merging of Kelvin-  
1352 Helmholtz vortices into large coherent flow structures in a high Reynolds number flow past a  
1353 wall-mounted square cylinder," *Ocean Engineering*, 2020.
- 1354 40 M. H. Ahmadi, "Influence of upstream turbulence on the wake characteristics of a tidal stream  
1355 turbine," *Renewable Energy*, vol. 132, pp. 989–997, 2019.
- 1356 41 C. H. Frost, P. S. Evans, M. J. Harrold, A. Mason-Jones, T. O'Doherty, and D. M. O'Doherty,  
1357 "The impact of axial flow misalignment on a tidal turbine," *Renewable Energy*, vol. 113, pp.  
1358 1333–1344, 2017.
- 1359 42 T. de Jesus Henriques, S. Tedds, A. Botsari, G. Najafian, T. Hedges, C. Sutcliffe, I. Owen, and R.  
1360 Poole, "The effects of wave-current interaction on the performance of a model horizontal axis  
1361 turbine," *International Journal of Marine Energy*, vol. 8, pp. 17–35, 2014.
- 1362 43 S. Tatum, C. Frost, M. Allmark, D. O'Doherty, A. Mason-Jones, P. Prickett, R. Grosvenor, C.  
1363 Byrne, and T. O'Doherty, "Wave-current interaction effects on tidal stream turbine performance  
1364 and loading characteristics," *International Journal of Marine Energy*, vol. 14, pp. 161–179, 2016.
- 1365 44 M. Allmark, *Condition Monitoring and Fault Diagnosis of Tidal Stream Turbines Subjected to  
1366 Rotor Imbalance Faults*. PhD thesis, School of Engineering, Cardiff University, 2016.
- 1367 45 C. Frost, *Flow Direction Effects On Tidal Stream Turbines*. PhD thesis, School of Engineering,  
1368 Cardiff University, 2016.
- 1369 46 T. Blackmore, L. E. Myers, and A. S. Bahaj, "Effects of turbulence on tidal turbines: Implications  
1370 to performance, blade loads, and condition monitoring," *International Journal of Marine Energy*,  
1371 vol. 14, pp. 1–26, 2016.
- 1372 47 T. Ebdon, D. O'Doherty, T. O'Doherty, and A. Mason-Jones. Modelling the effect of turbulence  
1373 length scale on tidal turbine wakes using advanced turbulence models. In *Proc. of 12th European  
1374 Wave & Tidal Energy Conference (EWTEC 2017)*, 27th Aug – 1st Sept. 2017.
- 1375 48 Fredriksson, S., Broström, G., Jansson, M., Nilsson, H., & Bergqvist, B. J. M. "Large eddy  
1376 simulation of the tidal power plant deep green using the actuator line method" *IOP Conference  
1377 Series: Materials Science and Engineering* vol. 276(1), pp. 012014, 2017

- 1378 49 Fredriksson, S. T., Brostrom, G., Bergqvist, B., Lennblad, J., & Nilsson, H. Turbulence  
1379 Characteristics in Tidal Flows Using LES and ALM to Model the Tidal Power Plant Deep Green.  
1380 In *Proc. of 4th Asian Wave & Tidal Energy Conference (AWTEC 2018)*, 9th-13th Sept. 2018.
- 1381 50 McCaffrey, K., Fox-Kemper, B., Hamlington, P. E., & Thomson, J. “Characterization of  
1382 turbulence anisotropy, coherence, and intermittency at a prospective tidal energy site:  
1383 Observational data analysis.” *Renewable Energy*” vol. 76, pp. 441—453, 2015.
- 1384 51 T. Ebdon, *The Impact of Turbulence and Turbine Operating Condition on the Wakes of Tidal  
1385 Turbines*. PhD thesis, School of Engineering, Cardiff University, 2019.
- 1386 52 H.K. Versteeg and W. Malalasekera. *An Introduction to Computational Fluid Dynamics, The  
1387 Finite Volume Method*. Pearson Education Limited, 2007.
- 1388 53 I.A. Milne, R.N. Sharma, R.G.J. Flay, and S. Bickerton. Characteristics of the turbulence in the  
1389 flow at a tidal stream power site. *Phil Trans R Soc A*, 371:20120196, 2013.
- 1390 54 T. Ebdon, D. O’Doherty, T. O’Doherty, and A. Mason-Jones. Simulating Marine Current Turbine  
1391 Wakes Using Advanced Turbulence Models. In *Proc. of 3rd Asian Wave & Tidal Energy  
1392 Conference (AWTEC 2016)*, 24th–28th Oct. 2016.
- 1393 55 P. R. Bevington and D. K. Robinson, *Data reduction and error analysis for the physical sciences*.  
1394 McGraw-Hill, 2003.
- 1395 56 National Institute of Standards and Technology, \e-Handbook of Statistical Methods."  
1396 <http://www.itl.nist.gov/div898/handbook/>, 2013. [Online; last accessed 23-August-2018].
- 1397 57 M. H. Baba-Ahmadi and P. Dong, “Numerical simulations of wake characteristics of a horizontal  
1398 axis tidal stream turbine using actuator line model,” *Renewable Energy*, vol. 113, pp. 669–678,  
1399 2017.

1400

1401 **Appendix:**

1402 **Table A.1:** Turbine performance metrics, all CFD runs. The velocity used for the calculations  
1403 of  $C_p$ ,  $C_T$  and  $C_\theta$  are the target velocities.

$v / \text{ms}^{-1}$	TI / %	$L_t / \text{m}$	$\lambda$	$C_p$	$C_T$	$C_\theta$	$\sigma_{C_p}$	$\sigma_{C_T}$	$\sigma_{C_\theta}$	run no.
1.1	5	0.25	2.5	0.35	0.67	0.14	0.0118	0.017	0.0047	1
1.1	5	0.25	3.65	0.43	0.85	0.12	0.0192	0.024	0.0052	2
1.1	5	0.25	4.5	0.41	0.89	0.09	0.0182	0.025	0.0041	3
1.1	5	0.50	2.5	0.35	0.67	0.14	0.0200	0.036	0.0080	4
1.1	5	0.50	3.65	0.44	0.86	0.12	0.0398	0.050	0.0109	5
1.1	5	0.50	4.5	0.42	0.90	0.09	0.0203	0.025	0.0045	6
1.1	5	1.00	2.5	0.35	0.67	0.14	0.0101	0.016	0.0040	7
1.1	5	1.00	3.65	0.43	0.85	0.12	0.0200	0.025	0.0055	8
1.1	5	1.00	4.5	0.41	0.89	0.09	0.0217	0.026	0.0048	9
1.1	10	0.25	2.5	0.35	0.67	0.14	0.0289	0.040	0.0116	10
1.1	10	0.25	3.65	0.41	0.82	0.11	0.0468	0.058	0.0128	11
1.1	10	0.25	4.5	0.44	0.92	0.10	0.0486	0.055	0.0108	12
1.1	10	0.50	2.5	0.34	0.66	0.14	0.0237	0.046	0.0095	13
1.1	10	0.50	3.65	0.44	0.86	0.12	0.0210	0.031	0.0057	14
1.1	10	0.50	4.5	0.44	0.93	0.10	0.0463	0.058	0.0103	15
1.1	10	1.00	2.5	0.34	0.66	0.14	0.0213	0.033	0.0085	16
1.1	10	1.00	3.65	0.43	0.85	0.12	0.0431	0.051	0.0118	17
1.1	10	1.00	4.5	0.44	0.92	0.10	0.0486	0.055	0.0108	18
1.1	20	0.25	2.5	0.36	0.70	0.14	0.0529	0.075	0.0212	19
1.1	20	0.25	3.65	0.43	0.84	0.12	0.0815	0.100	0.0223	20
1.1	20	0.25	4.5	0.43	0.91	0.10	0.1086	0.126	0.0241	21
1.1	20	0.50	2.5	0.33	0.65	0.13	0.0407	0.061	0.0163	22

1.1	20	0.50	3.65	0.50	0.91	0.14	0.1304	0.151	0.0357	23
1.1	20	0.50	4.5	0.44	0.92	0.10	0.1121	0.135	0.0249	24
1.1	20	1.00	2.5	0.33	0.65	0.13	0.0447	0.081	0.0179	25
1.1	20	1.00	3.65	0.42	0.83	0.12	0.0878	0.107	0.0241	26
1.1	20	1.00	4.5	0.40	0.88	0.09	0.0653	0.080	0.0145	27
1.02	11.7	0.19	2.5	0.33	0.66	0.13	0.0365	0.070	0.0146	28
1.02	11.7	0.19	3.65	0.44	0.85	0.12	0.0678	0.090	0.0186	29
1.02	11.7	0.19	4.5	0.42	0.90	0.09	0.0802	0.102	0.0179	30
1.03	17.5	0.43	2.5	0.34	0.68	0.14	0.0728	0.136	0.0292	31
1.03	17.5	0.43	3.65	0.45	0.86	0.12	0.1105	0.144	0.0303	32
1.03	17.5	0.43	4.5	–	–	–	–	–	–	33
1.5	1.75	0.50	1.5	0.14	0.49	0.10	0.0028	0.010	0.0019	34
1.5	1.75	0.50	2.5	0.35	0.67	0.14	0.0074	0.010	0.0030	35
1.5	1.75	0.50	3	0.42	0.79	0.14	0.0062	0.009	0.0021	36
1.5	1.75	0.50	3.65	0.44	0.86	0.12	0.0081	0.010	0.0022	37
1.5	1.75	0.50	4	0.44	0.88	0.11	0.0148	0.017	0.0037	38
1.5	1.75	0.50	4.5	0.42	0.90	0.09	0.0158	0.018	0.0035	39
1.5	1.75	0.50	5.5	0.33	0.90	0.06	0.0164	0.019	0.0030	40

1404

# **The Impact of Turbulence and Turbine Operating Condition on the Wakes of Tidal Turbines**

T Ebdon, M Allmark, D O'Doherty A Mason-Jones, T O'Doherty  
Cardiff Marine Energy Research Group, Cardiff University, Cardiff

G Germain and B Gaurier  
IFREMER, Marine and Structures Laboratory, Centre Manche Mer du Nord,  
Boulogne-sur-Mer

## **Highlights**

- Wake widths and lengths for a tidal turbine using three different analysis metrics are presented.
- Three levels of turbulent conditions are presented using upstream grids.
- The impact of the turbine operating conditions, on the wake characteristics, are analysed.
- The impact of turbulence intensity and Integral length scales on the wake characteristics are analysed.

**Declaration of interests**

The authors declare that they have no known competing financial interests or personal relationships that could have appeared to influence the work reported in this paper.

The authors declare the following financial interests/personal relationships which may be considered as potential competing interests:

Journal Pre-proof